

Using the World Wide Lightning Location Network (WWLLN) to study Very Low Frequency transmission in the Earth-Ionosphere Waveguide: 2. Model test by patterns of detection/non-detection

Abram R Jacobson¹, Robert H. Holzworth¹, and James B Brundell²

¹University of Washington

²University of Otago

November 24, 2022

Abstract

This is the second half of a two-part study. In the first part, we had used the World Wide Lightning Location Network's recorded signal amplitudes to test a model of Very Low Frequency signal transmission from the lightning to each sensor. The model predicts a dramatic worsening of transmission at low magnetic latitudes, for nighttime propagation (compared to daytime propagation) toward magnetic West. However, we found that the use of amplitudes was ill-adapted for testing the model under conditions of a deep outage of transmission. Since the relative weakening of nighttime transmission is rather counter-intuitive, we have now developed an alternative approach to testing that model prediction. This alternative approach highlights the patterns of detection/non-detection of several low-magnetic-latitude WWLLN stations and compares those patterns with the appropriate patterns of the model transmission.

Using the World Wide Lightning Location Network (WWLLN) to study Very Low Frequency transmission in the Earth-Ionosphere Waveguide: 2. Model test by patterns of detection/non-detection

Abram R. Jacobson¹ and Robert H. Holzworth

Earth and Space Sciences Dept., University of Washington, Seattle U. S.

and

James B. Brundell

Physics Dept., University of Otago, Dunedin NZ

1: Corresponding author Abram R. Jacobson, abramj@uw.edu

Abstract

This is the second half of a two-part study. In the first part, we had used the World Wide Lightning Location Network's recorded signal amplitudes to test a model of Very Low Frequency signal transmission from the lightning to each sensor. The model predicts a dramatic worsening of transmission at low magnetic latitudes, for nighttime propagation (compared to daytime propagation) toward magnetic West. However, we found that the use of amplitudes was ill-adapted for testing the model under conditions of a deep outage of transmission. Since the relative weakening of nighttime transmission is rather counter-intuitive, we have now developed an alternative approach to testing that model prediction. This alternative approach highlights the patterns of detection/non-detection of several low-magnetic-latitude WWLLN stations and compares those patterns with the appropriate patterns of the model transmission.

Key points

Prior knowledge: Low-magnetic-latitude Very Low Frequency radio transmission in the Earth-Ionosphere Waveguide is suppressed for propagation toward magnetic West, relative to magnetic East.

New finding: This magnetic-westward suppression is dramatically stronger during night than during day.

New finding: The magnetic-westward suppression at night applies to nearly the entire westward half-plane, from magnetic-South clockwise to magnetic-North.

New finding: The magnetic-westward suppression at night is readily observable for dip angles in the range -30 deg to +30 deg.

Index terms: 2487, 6934, 6964,

1. Introduction

This is not a new topic. East-west asymmetry in VLF (Very Low Frequency; 3-30 kHz) propagation in the Earth-Ionosphere Waveguide had been inferred as early as the 1920's [see the historical review by *Crombie* , 1958]. The geomagnetic control over VLF propagation is expected to depend strongly on two orientational parameters [*Budden* , 1985; *Piggott et al.* , 1965; *Pitteway* , 1965; *Wait and Spies* , 1960; *Wait and Spies* , 1964; *Yabroff* , 1957]. One is the dip angle of the geomagnetic field, and the other is the propagation magnetic azimuth of the VLF wavefield. Along any long-range propagation Great Circle Path, both of these orientational parameters can widely vary. Thus, e.g., it is only very approximate to characterize the propagation magnetic azimuth "of the path" by its value at a path endpoint. The research results we review below can be broadly separated as to whether they just grossly consider the whole path together, or whether they dissect the path into small segments and use a different propagation azimuth and magnetic dip within each segment. The former we will call "bucket" approaches, in that they just characterize the entire path as being effectively at one propagation magnetic azimuth. By contrast, the model comparisons which consider the local nature of the two orientational parameters will be called "local" approaches.

All studies of the azimuthal asymmetry of VLF propagation prior to the present have been based on observing the effect of magnetic propagation azimuth on received amplitudes. This is equally true when the signals received were from narrow-band artificial beacons [e.g., *Bickel et al.* , 1970; *Pappert and Hitney* , 1988] or when derived from lightning strokes [e.g., *Hutchins et al.* , 2013; *Jacobson et al.* , 2021; *Taylor* , 1960]. In the already-published [*Jacobson et al.* , 2021] first half of the present study, henceforth referred to as "JHB1", we followed the amplitude-comparison approach. However, we reached a cul-de-sac with that approach, when we tried to test a particular non-intuitive though impactful prediction of our model [*Jacobson et al.* , 2010; *Jacobson et al.* , 2009; *Jacobson et al.* , 2012]. The prediction is that for propagation at low dip angle, e.g. in the range -30 to +30 deg, propagation toward the magnetic West is deeply attenuated during dark-path conditions (night), *relative to sunlit-path (day) conditions* . Curiously, this counter-intuitive effect had not been overtly remarked prior to JHB1, though the physics package of the comprehensive, state-of-the-art path simulator, LWPC [*Pappert and Ferguson* , 1986], certainly contains all the relevant physics.

We found in JHB1 that the sought-after dark-path conditions apparently caused such a dearth of numerically sufficient lightning detections at the pertinent stations, so that amplitudes could not be determined with statistical accuracy. Thus JHB1 could not test its most interesting model prediction. "No detection, no amplitude".

This shortcoming of JHB1 motivated the present study, which is the second part of the study begun by JHB1. We completely change strategy in this paper. Rather than comparing amplitudes, we examine observed statistical patterns of detection/non-detection from ten selected stations. We compare those patterns to predictions of the model. The stations are chosen to represent all longitude sectors and all Universal Times, and to include many diverse paths from the lightning locations to the stations, in such a manner as to provide compelling statistical evidence on the model's predictions. The number of paths included exceeds 15-billion. Each of these paths is then dissected into 50 path segments, for a grand total exceeding 750-billion

path segments. At each path segment, the geomagnetic dip angle and magnetic propagation azimuth are calculated, along with the instantaneous solar zenith angle, are combined to predict the modeled contribution of that path segment to the overall integrated attenuation for that path.

2. Background

2a. Prior observations of east-west asymmetry of VLF propagation

Here we review the carefully documented work that began in the 1950's. Crombie described new measurements performed in New Zealand during 1957 [Crombie , 1958], one purpose of which was to investigate the asymmetry earlier hinted at by the scattered results of the 1920's. The 16.6-kHz signal from a powerful transmitter ("GBR") in Rugby, UK was received by a magnetic loop and a vertical aerial at Wellington, NZ. The receiver and the transmitter were nearly antipodal. By rotating the loop antenna, Crombie was able to select separately the signal arriving on either Great Circle Path, from respectively NNW or SSE (reckoned at Wellington.) The signal strength on each orientation of the loop was measured versus time during three multi-day periods. The results confirmed not only that the signal arriving from the NNW had 10-15 dB stronger amplitudes than the path arriving from the SSE, but also that the diurnal variations were dissimilar between the two paths. Crombie attributed this difference to the east-west components of each path, although this was left notional. The detailed variation of the magnetic azimuth along each path was not presented or addressed, so that Crombie's work was in the "bucket" category. The diurnal variation was not explained, but the gross difference between eastward and westward propagation was noted.

Shortly after the work by Crombie, there was a systematic attempt to use geolocated lightning to observe the zonal asymmetry of long-range broadband VLF propagation [Taylor , 1960]. Whereas Crombie had relied on a discrete, narrow-band, man-made beacon, Taylor exploited the powerful broadband emissions of lightning return strokes. Attention was focused on daytime conditions, with most of the paths over seawater. VLF receiver stations in the western United States and in Hawaii, triggering off common lightning strokes, were used to crudely geolocate the lightning, at least within <10% of the path length, by triangulating the direction found at each station. Each station measured and recorded the vertical electric field with a vertical mast, and also provided the direction of arrival from comparing signals on two vertical-magnetic-loop antennas. As was necessary in that era, data were recorded for off-line analysis using oscilloscopes and cameras. The east-to-west attenuation from twenty lightning discharges was used to determine a mean spectral attenuation (dB/1000km) for that direction of propagation. The spectral attenuation was determined for the entire VLF band. Similarly, the spectral attenuation for west-to-east attenuation was determined using sixteen lightning discharges. All observations were for entirely-daylit paths. It was found that attenuation east-to-west exceeded attenuation west-to-east, by approximately 3 dB/1000km for $f < 8$ kHz and by approximately 1 dB/1000km for $f > 10$ kHz.

Taylor's characterization of the paths as "east to west" versus "west to east" [Taylor , 1960] is in the bucket category. Moreover Taylor did not consider the control by geomagnetic dip angle; rather, all the paths were simply tagged as "east to west" or as "west to east", regardless of magnetic dip, and then simply labeled with one orientation. The lightning locations are not given [Taylor , 1960], so it would not be possible to retrospectively model Taylor's observations with a more local approach.

In 1969, the United States Naval Ocean Systems Center conducted airborne measurements of VLF beacon signals on Great Circle Paths from the island of Hawaii toward San Diego and from the island of Hawaii toward Wake. The paths were, respectively, west-to-east and east-to-west paths, entirely over seawater, and entirely nighttime. These data were later presented and compared [Pappert and Hitney , 1988] to state-of-the-art, full-wave waveguide propagation calculations using the LWPC [Pappert and Ferguson , 1986]. The fixed frequencies of the beacons at Hawaii were discretely between 10.9 kHz (the lowest) and 28.0 kHz (the highest). The airborne receiver recorded signal amplitudes due to the multifrequency sounder for the first ~4000 km of each path. Thus the measurements were all done within 4000 km of Hawaii. The VLF data were compared to a model that included detailed tracking of the propagation azimuth and the magnetic dip angle locally at all points along the propagation path. This was a local approach, and was a critical advance

over the bucket approach. It was found that the eastbound (San Diego path) signal was very reproducible day-to-day, and was essentially perfectly modeled by LWPC with a generic nighttime profile [Pappert and Hitney, 1988]. The westbound (Wake path) signal, by contrast, was more variable day-to-day, and this adversely affected the agreement with the model, although on average the agreement was satisfactory. The variability for westbound propagation was speculated to be related to sporadic electron-density features near altitude 90 km. We note that the sampled paths did not delve lower than about 30 deg in dip angle.

In addition to the airborne measurements using the multifrequency beacon, the same aircraft was also deployed to measure the signal from the unique 23.4-kHz signal "NPM" radiated from the area of Honolulu, Hawaii with much higher power than the research multifrequency beacon. The NPM signal was measured along Great Circle Paths from NPM toward Seattle, Ontario (California), Samoa, and Wake Island. Results were reported [Bickel et al., 1970], similarly, out to ~ 4000 km range, and were entirely over seawater and at night. The authors [Bickel et al., 1970] used an early predecessor of LWPC to compare with waveguide theory, and found that the model predictions of dependence on magnetic azimuth and magnetic dip angle were robustly confirmed at 23.4 kHz by the airborne measurements. Their model comparison was a local approach, exactly similar to that used for the multifrequency beacon data [Pappert and Hitney, 1988].

A more recent entry into the observation of propagation magnetic-azimuth asymmetry was done with the World Wide Lightning Location Network, or WWLLN [Hutchins et al., 2013]. It dealt with over-seawater paths in the Pacific sector, using WWLLN stations at island locations Suva, Tahiti, and Honolulu. This study is in the "bucket" category. The study used lightning strokes jointly detected by all three of those stations (along with other stations as well.) Each lightning stroke's radiated VLF energy was determined with the WWLLN energy retrieval described elsewhere [Hutchins et al., 2012]. The candidate strokes were selected according to the following strict limiting criteria:

- (a) The WWLLN VLF energy determination for the stroke needed to have an estimated error less than 10% of the VLF energy.
- (b) The stations participating in the location/energy determination needed to be equally distributed east/west of the stroke location, to within 25%.
- (c) The strokes were limited to those for which the three paths to Suva, Tahiti, and Honolulu were *all* either less than 5% daylight or more than 95% daylight.

The strokes were selected from those occurring from May 2009 to May 2013. With these criteria, only 0.2% of the stroke population was accepted, that is, only 2×10^6 strokes were accepted.

The high-confidence energy retrievals for the 2×10^6 accepted strokes allowed each of these stroke's "normalized electric field" to be derived for each stroke, so as to use all the strokes despite their widely differing stroke VLF energies [Hutchins et al., 2013]. The normalization was the rms measured electric field (in units of μVm^{-1}) divided by the square root of the retrieved VLF energy (in units of J). This normalization was tabulated for each of the strokes as the electric field in dB above $1 \mu\text{Vm}^{-1}\text{J}^{-1/2}$.

The 2×10^6 accepted strokes were grouped into azimuth/distance bins, with eight azimuth bins, each 45 deg wide, and distance bins 500 km wide. The azimuth was the average magnetic azimuth over the path, which is approximate, as the azimuth actually varies along each path. Within each bin, the bin median was used to show variations versus distance and azimuth. In order to highlight azimuthal variation, each attenuation rate was normalized by an "all-azimuth" average. Thus the normalized-attenuation data vary azimuthally with a mean of unity. The normalized-attenuation data were compared to the standard theory of idealized sharp-boundary reflection from a magnetized D-layer [Wait and Spies, 1960]. The agreement between the WWLLN results and the sharp-boundary model was rather good [see Figure 5 in Hutchins et al., 2013]. In part this agreement may be fortuitous. The model uses simply a sharp-boundary ionosphere, which is a problem. Moreover, the model did not explicitly treat "day" or "night", but rather tried two electron densities. However, the cited model stuck with $2 \times 10^7 \text{ s}^{-1}$ as the fixed collision electron-neutral rate in the case of either of those electron densities, so they really do not illuminate the difference between night and

day reflection conditions. Another cause for caution at the good agreement between the model and the data is that the model was for dip angle of 0 deg, whilst the range of dip-angle magnitude in the paths in the WWLLN study was 0 deg to ~ 45 deg. Therefore it is not ruled-out that the good agreement of the Wait model and the WWLLN data may have been partially fortuitous.

The legacy results cited above concern direct measurements of the VLF amplitude. We now mention a different set of observations in which east-west asymmetry, or "non-reciprocity", was revealed: The several observations of VLF modal interference for narrow-band transmissions. Here for brevity we mention only a few of these reports, because our case (broadband emissions from lightning) has wide enough bandwidth to essentially wash-out any mode-interference effects. WWLLN's passband of useful VLF energy is roughly 5-20 kHz [see, e.g., Figure 2.2 in *Hutchins*, 2014]. This mixes interferences of different spatial scale, so that the net result is washed-out.

An early series of measurements on modal interference [*Crombie*, 1966] documented markedly different modal-interference wavelengths for several discrete frequencies from 18 to 24 kHz. A more recent study [*Samanes et al.*, 2015] lacked westward paths and thus could not address this non-reciprocity issue. An even more recent study [*Chand and Kumar*, 2017] did not yield unambiguous results on non-reciprocity.

2b. Prior modeling of east-west asymmetry of VLF propagation

The reflection of radio waves from the underside of the ionosphere became an active area of research during the 1950s [see the historical references given by, e.g., *Barber and Crombie*, 1959; *Wait and Spies*, 1960; *Wait and Spies*, 1964; *Yabroff*, 1957]. The problem was nontrivial due to the anisotropy of the dielectric, associated with the gyration of charged particles about the geomagnetic field. This was especially true for VLF waves, whose height of reflection occurs in the lowermost ionosphere, namely the D-layer. The strong electron-neutral collision rate in the D-layer further complicates models of VLF reflection. The models needed to address practical challenges, e.g.:

- (a) What is the VLF reflectivity?
- (b) How does it depend on solar zenith angle?
- (c) How does the reflectivity depend on angle-of-incidence?
- (d) How does the reflectivity depend on local propagation magnetic azimuth (reckoned clockwise from local magnetic North) and on local magnetic declination ("dip angle")?
- (e) How does the reflectivity depend on electron-neutral collision rate?

Starting late in the 1950's, sharp-boundary treatments of the collisional, anisotropic VLF reflection process were set up analytically and solved numerically with newly available digital computers [*Barber and Crombie*, 1959; *Wait and Spies*, 1960; *Wait and Spies*, 1964; *Yabroff*, 1957]. The first numerical model of an arbitrarily-layered (rather than just a sharp boundary) D-layer [*Piggott et al.*, 1965; *Pitteway*, 1965] followed quickly, although its physical implications appear to have been only slowly appreciated. The Pitteway model for the continuously varying D-layer solved the Maxwell Equations for the altitude-dependent, anisotropic, and complex susceptibility tensor. All of the sharp-boundary models, as well as the Pitteway model, dealt with the elementary reflection of an incident plane wave.

Such plane-wave models are excellent for providing insights on "process" questions, such as those cited in the previous paragraph. However, for long-range "multi-hop" propagation, it is more efficient, though less heuristically instructive, to cast the problem in terms of waveguide modes in the spherical-shell Earth-ionosphere waveguide (EIWG). The modes are akin to cylindrical waves from a point source within a parallel-plane waveguide, except that the waveguide elements are (approximately) *concentric spherical surfaces* [see the illuminating tutorial by *Cummer*, 2000]. A waveguide model provides a point-to-point complete description of the VLF transmission along any given Great Circle path. This includes all portions of the path. The first portion consists of 3-dimensional expansion of the wavefield into a hemisphere. The next portion takes account of the first ionospheric reflection, which effectively is a transition to spherical-shell EIWG propagation.

This transition needs many higher-order modes to describe the wavefield, because at such a short range (e.g., < 1000 km) a broad range of plane-wave "angles of incidence" are at play [Cummer, 2000]. Ultimately, however, at longer range the waveguide modes simplify. For a vertical-dipole source near ground level, and a vertical-dipole receiver also near ground level, the modes simplify at large distances to the fundamental Transverse Magnetic (TM) mode. Thus the transmission characteristics vary from 3-dimensional expansion into a hemisphere, to a single 2-D, fundamental TM mode in the waveguide.

The waveguide approach was perfected in the Long Range Propagation Capability, or LWPC [Pappert and Ferguson, 1986] suite of computer codes developed by the United States Navy. The LWPC includes an atlas of Earth-surface conductivity. The user can select a D-layer model, usually exponential profiles of electron density and of electron-neutral collision rate. The LWPC contains "everything" in one master code suite. LWPC uses just an approximation of the D-layer electron-density profile, but that is justified by the impossibility of knowing any better profile at any given instant.

One adverse side-effect of its end-to-end completeness is that the LWPC blurs (to the LWPC user) the role of *local* parameters, such as solar magnetic propagation azimuth and local magnetic dip angle. These vary along the path, but the LWPC's end-to-end approach path-integrates over their local variations, and all the user sees is the result of the path integration. Thus, despite its completeness, premiere accuracy, and reliability, the LWPC is not pedagogically illuminating for exploring individual local *processes* in isolation.

3. Recap of part 1 of the present study

3a. Plane-wave reflectivity and path transmission

This article is part 2 of a two-part study; here, we briefly recap the results of the first part, from JHB1. The work to follow entirely depends on JHB1, and the reader should refer to that published article for details beyond the brief recap here.

We rely on a numerical model of plane-wave reflection from a diffuse, collisional, anisotropic D-layer [Jacobson *et al.*, 2010; Jacobson *et al.*, 2009; Jacobson *et al.*, 2012]. Our model is a modernization of Pitteway's groundbreaking treatment [Piggott *et al.*, 1965; Pitteway, 1965]. We represent the electron-neutral collision rate by an exponentially declining function of altitude as is common in this field. For the electron density, we use an exponentially increasing function of altitude, also common in the field [see, e.g., Eq. 3.23, Section 3.2.3, in Volland, 1995]. See Table 1 for details.

Figure 1 summarizes the prediction of our plane-wave reflection model. The vertical axis is the amplitude reflection coefficient, R , from the D-layer for a typical long-range-propagation angle of incidence, in this case chosen as 85 deg. The reflection coefficient shown has been averaged over all frequencies from 5 to 20 kHz. As shown in JHB1, R varies continuously with solar zenith angle, but we show the pure-day and pure-night extreme cases only. On the left of Figure 1 is shown (a) the day-profile D-layer result, while on the right is shown (b) the night-profile D-layer result (refer to Table 1 for profile parameters). The abscissa is the wave magnetic propagation azimuth. A separate curve is shown for each abs(dip angle), from 5 deg (blue) to 85 deg (red), in steps of 5 deg. The curves for dip = 30 deg and 45 deg are labeled in the night profile. For both (a) and (b), the curve for dip = 45 deg is dashed. The horizontal black line marks the nadir of the night-profile reflectivity level for dip = 45 deg.

How do we employ the single-reflection reflectivity from a plane-wave model, in the context of long-range ("multi-hop") propagation of quasi-cylindrical waves in a spherical-shell waveguide? The article on the first half of this project, JHB1, shows how this is done heuristically but with satisfactory agreement with observations: First, we correct the wave amplitude for the varying cross-sectional area of a ray-bundle on the spherical Earth (see Eq. 7 in JHB1). Second, we rely in JHB1 on a free parameter " r ", which is the effective number of reflections per reference distance $\rho_0 = 1000$ km (= 1 Mm). In JHB1 we demonstrated how comparison with observed received electric-field amplitude resulted in a fit for r in the range $3 > r > 2$.

Those two heuristics (correcting for the ray-bundle area, and invoking an effective reflection-per-pathlength) were used in JHB1 to crudely approximate long-range waveguide transmission in terms of the single-hop,

plane-wave reflectivity model. We define a "logarithmic reference transmission", *assuming perfect ground conductivity*, along the Great Circle Path segment $L_{i,m}$ from VLF emission point "m" to sensor point "i":

$$\ln(\text{ref. transmission}) = \frac{1}{\rho_0} \int_0^{L_{i,m}} \ln(R[Z_{i,m}(t_0), \alpha_{i,m}, I_{i,m}]) ds_{i,m} + C(L_{i,m}) \text{Eq. (1)}$$

where

$L_{i,m}$ = arcdistance along Great Circle Path from lightning location m to station i

$Z_{i,m}(t)$ = time-dependent, location-dependent solar zenith angle along path i,m

$\alpha_{i,m}$ = location-dependent magnetic propagation azimuth along path i,m

$I_{i,m}$ = location-dependent magnetic dip angle along path i,m

$R(Z_{i,m}(t), \alpha_{i,m}, I_{i,m})$ local instantaneous plane-wave reflectivity

$ds_{i,m}$ = differential path element along Great Circle Path i,m

$\rho_0 = 1000$ km

The term $C(L_{i,m})$ in Eq. (1) is the geometrical correction due to the variation of ray-bundle cross-sectional area. We tabulate the correction, relative to its value at the reference distance 1000 km:

$$C(L_{i,m}) = \ln \left\{ \sqrt{\frac{\sin(\rho_0/R_E)}{\sin(L_{i,m}/R_E)}} \right\} \text{Eq. (2)}$$

where R_E is the Earth's radius.

The logarithmic reference transmission (Eq. 1) must be multiplied by the fitted parameter r to give an estimate of the actual logarithmic path transmission *assuming zero ground losses* (see Eq. 9b in JHB1). This r parameter was fitted to lie in the range of 2 to 3. Physically, it is the number of hops per 1000 km reference distance, subject to our model's assumption of 85-deg angle-of-incidence.

Ignoring ground losses would be unacceptable if we were trying to calculate absolute transmission in the waveguide. However, our application involves examining the difference between day and night conditions on the propagation anisotropy. The ground conductivity effects are unchanged (on a given path) between day and night. Thus modeling only D-layer losses is a satisfactory (though not perfect) approach for our study of day-versus-night differences.

A further convenient simplification introduced in JHB1 is that we actually solve for the log reflectivity $\ln(R)$ only for the two extreme cases of pure day and pure night. Any intermediate case is approximated by a linear combination of pure-day and pure-night, using a smooth function of solar zenith angle (see Eqs. 10-11 in JHB1). *This is done locally, at each point along the path integral in Eq. (1), and for local solar zenith angle obtaining at the instant of the lightning stroke.* There is a crucial difference between, on the one hand, making the linear combination locally (which we do), versus, on the other hand, evaluating the path integral along the entire path both for an artifactual day and an artifactual night case, then taking a linear combination of those two results based on the proportion of the path that is daylit. The approach latter would be clearly incorrect.

3b. Disfavoring of nighttime (relative to daytime) magnetic-westward propagation

Note that for $\text{abs}(\text{dip angle}) < 45$ deg, the night-profile reflectivity (Figure 1b) for propagation toward magnetic west (270 deg) is *less than the day-profile reflectivity (Figure 1a)*. This favoring of daytime over nighttime transmission for $\text{abs}(\text{dip angle}) < 45$ deg actually applies over a broad azimuth sector centered on magnetic west. Thus, for essentially half of all possible dip angles, and for essentially half of all possible propagation magnetic azimuths, the *nighttime reflection is predicted by our model [Jacobson et al., 2010; Jacobson et al., 2009] to be disfavored relative to the daytime reflection, and for small dip angle deeply disfavored*. This surprising and counter-intuitive feature is not remarked elsewhere in the VLF literature, and thus the burden is on us to provide observational support for this counter-intuitive claim. Intuition would

suggest that nighttime propagation should be *less* lossy than daytime, because the nighttime reference height (85 km in our model) has only 17% as much electron-neutral collision rate as does the daytime reference height (73 km in our model).

The remainder of this article relies on the first part of the study (JHB1) for a detailed development of the model theory. Readers should consult JHB1, which was published as Open Access and hence is without cost to the reader.

3c. Summary of observational results from part 1 of the present study

We presented in JHB1 a method to study the behavior of the inter-station ratio of VLF stroke amplitudes, for strokes that are simultaneously recorded at multiple WWLLN stations. This approach combined numerous recurrent strokes from long-duration lightning clusters to build a time-series of the ratio for a major portion of the UT day. The time variations of the sliding-averaged ratio are dominated by transient excursions coinciding temporally with those periods when the solar terminator is present along one or both of the paths. See, e.g., Figure 2 in JHB1. This strongly motivates a model incorporating significant control by the solar zenith angle.

Our plane-wave model predicts that magnetic-westward propagation has less waveguide transmission than does magnetic-eastward propagation. *Crucially, the anisotropy is extremely magnified for a night ionosphere.* This anisotropy is modulated by magnetic dip angle: The anisotropy is strongest at low dip angle, and weakest at large dip angle.

To account for solar-zenith-angle control on the waveguide transmission, our model takes a weighted combination of pure-day and pure-night solutions, *determined locally for every path element along the Great Circle Path from the lightning to the WWLLN station, and for the exact Universal Time of the stroke* .

The model solution based on the plane-wave-reflection theory successfully accounted for the gross features of the solar-terminator transients; see, e.g, Figures 7-10 in JHB1.

Our model predicts, counter-intuitively, that the magnetic-westward attenuation at low magnetic latitude will be much deeper during night than during day conditions. Unfortunately, this suppression of magnetic-westward propagation also largely eliminates the availability of sufficiently numerous recurrent recordings of those signals at our low-latitude stations. Thus the amplitude-ratio method pursued in JHB1 was inherently unable to check on the model's most intriguing and counter-intuitive prediction.

Thus our method to follow, rather than using lightning detections that exist, is designed to demonstrate the pattern of where and when detections do *not* exist.

4. WWLLN evidence on day/night differences in anisotropic VLF propagation

4a. WWLLN database

The overall epoch for this study is 1 December 2009 through 31 May 2021, Universal Time (UT). Within that overall epoch, numerous WWLLN recording stations began operation, occasionally interrupted operation, and (in a few cases) ceased operation. For much of the overall epoch, at any time WWLLN had > 50 active stations worldwide. At present (2021) the census is > 60 active stations.

Our methodology in the following is to develop statistics on the *patterns of detection and non-detection by selected stations*. We use the entire WWLLN network product to define the overall population of WWLLN-located lightning strokes. This population is defined in a separate day file for each UT day. We then focus on ten selected stations located at magnetic low and mid latitudes. We develop statistical maps of the detection/non-detection of the overall WWLLN stroke population, by each of these ten selected stations.

To clarify "detection", we mean that a particular stroke is "detected" by a particular station *if that station participates in the solution for that particular stroke's location* . This is a stringent definition of "detection", compared to a more permissive definition that the station records a signal (whether or not that signal has the requisite amplitude and signal-to-noise to allow participation in the network solution.) The problem with

the permissive definition is that one can never be sure, or even reasonably sure, that a signal is associated with a given stroke, if that signal cannot be used in the position/time solution for that stroke.

Table 2 lists pertinent metadata about the ten selected stations. Three of the stations (Atuona, Tahiti, and Honolulu) are in the Pacific ocean and have dominantly over-seawater paths from abundant lightning in both their Eastern and Western sectors. Another station (Costa Rica) is on a relatively narrow land bridge between major oceans. Two stations (Peru and Dakar) are on the western periphery of lightning-rich continents.

For the statistics on each of the ten selected stations, we define a latitude band within which to include WWLLN strokes. This band is -40 to $+40$ deg N for nine of the stations, but for Honolulu the band is displaced to -30 to $+50$ deg N, in order to include the strokes in the northern continental United States. The population of WWLLN strokes within the latitude band is used to detect detection/non-detection by the respective selected station.

The population of WWLLN strokes within the latitude band and available for detection by the respective selected station varies from a maximum of $> 2 \times 10^9$ strokes (for both Honolulu and Tel Aviv) down to 3.2×10^8 strokes (for Belem). This disparity is driven mainly by the difference between the number of operating days for Honolulu (3873) or for Tel Aviv (3987), versus for Belem (566) within the overall epoch.

4b. Qualitative demonstration of geomagnetic and zenith-angle control over detection

Before embarking on a systematic quantitative analysis, we show a qualitatively clear example of the control over detection exerted by solar zenith angle and by geomagnetic parameters. Figure 2 shows the case of Atuona station, near the mid-Pacific. This example conveniently illustrates the situation for low dip angle and nearly-zonal magnetic propagation azimuth everywhere along the paths eastward and westward to regions of abundant lightning. In Figure 2, the station is a black rectangle symbol. In Figure 2(a), to the East of Atuona is shown a red rectangular box in northwestern South America. We select all WWLLN strokes within that box. For each stroke within that box, we calculate the solar zenith angle (at D-layer height) for all points along the path to Atuona from the stroke, and characterize each stroke by the proportion of the path that is in daylight. Figure 2(b) shows the daylit-fraction distribution of all strokes in the red box of Figure 2(a). The distribution is flat except for roughly equal peaks both at pure-dark (daylit fraction = 0) and at pure-daylit (daylit fraction = 1). We now ask, what is the Atuona detection efficiency (DE) for these strokes, versus the daylit fraction parameter? This is shown in Figure 2(c). The DE peaks toward maximum daylight, and is suppressed (by an order of magnitude) for daylit fraction < 0.6 .

Now let us define a "control" case, which is shown in the right column of Figure 2. Figure 2(d) shows in red a "West box" over the Australasia sector. It is slightly further from Atuona than the East Box, but is roughly comparable in dip angle along the paths to Atuona. Figure 2(e) shows the daylit-fraction distribution for all strokes in the West box. Figure 2(f) shows the DE for Atuona detection of those strokes, as a function of daylit fraction. Now the DE for eastward propagation is relatively indifferent to daylit fraction, and the median DE for the west box is two orders-of-magnitude higher than the median DE for the East box (Figure 2c), and one order-of-magnitude greater than the maximum DE for the East box (Figure 2c). We note that this is a case where the paths to Atuona from either the West or the East box are everywhere quasi-zonal in magnetic azimuth, and are everywhere at very small dip angle (-20 deg to $+20$ deg). We chose this because of its convenience for a qualitative exercise like Figure 2.

This example qualitatively demonstrates, within the context of low dip angle, (a) the dramatic difference between propagation at eastward magnetic azimuth versus westward magnetic azimuth, and (b) the extreme favoring of daylit propagation over night propagation for westward magnetic azimuth. This latter feature has not previously been remarked in the VLF literature.

4c. Geomagnetic context for the ten selected stations

We now show the geomagnetic context of each of the ten selected stations and of the propagation paths connecting them to lightning strokes in their respective latitude band described in Table 2. The geomagnetic

model is the International Reference Geomagnetic Field, or IGRF [V-MOD, 2010]. Figure 3 contains a separate panel for each of the ten stations. Color indicates the geomagnetic dip angle’s absolute value, in deg. Black is dip = 0 deg. For nine of the panels, red is 74 deg, while for one (Figure 3i, Honolulu) the band is offset and the maximum dip angle is 76 deg. In addition to color-coding, discrete curves of $|\text{dip}| = 30, 45$ deg are overlaid on the map. The station is marked with a rectangle symbol, either white or black, to contrast with its immediate background color. The color shading covers the latitude band in which strokes are considered for detection/non-detection by the respective station.

Because of the extremely low transmission of VLF over Antarctic (or, to a lesser extent, Arctic) ice, we wish to exclude strokes whose Great Circle paths to the selected station reach further poleward than geographic latitude ± 55 deg. This excludes strokes roughly within a cone centered on the respective station’s antipode, which we blank-out with white. Thus, for example, in Figure 3(a) the antipode of Atuona is situated near the southern Red Sea. Each station has its own antipode, and cone centered there, in which we do not gather statistics regarding stroke detection by that station.

Recall that the model results (Figure 1) predict a nighttime increase of attenuation for propagation toward magnetic West, relative to daytime, for $|\text{dip angle}| < 45$ deg. This nighttime increase in attenuation toward magnetic West becomes especially severe for $|\text{dip angle}| < 30$ deg. Figure 3 shows visually that this band of enhanced nighttime westward attenuation occupies most of the important lightning prone areas [Christian *et al.*, 2003], excepting only the continental United States. That is, the nighttime disfavoring of magnetic-westward VLF propagation is not going to be a mere academic curiosity confined to a small region, but rather applies to most regions of relevance to global VLF lightning location.

4d. Spatial patterns of observed and predicted detectability

4d.1 Approach

We now start a formal comparison of the observed and predicted detection patterns of each of the ten selected stations. Separately for each station, we define two cohorts of strokes within the accepted latitude band. The first cohort contains the strokes whose Great Circle Paths to the station are $> 80\%$ sunlit at the instant of the stroke, at D-layer height. This first cohort represents mostly-daytime propagation. The second cohort contains the strokes whose Great Circle Paths to the station are $< 20\%$ sunlit, representing mostly-nighttime propagation.

In addition to those statistics based on observation, we calculate the logarithmic reference transmission (Eq. 1 above) for each Great Circle Path under two artificial conditions: that the entire path be either in daylight or in darkness. These yield "day" and "night" logarithmic reference transmissions.

Finally, we calculate the instantaneous logarithmic reference transmission, *using the actual instantaneous solar zenith angle at each point along each path*, for all strokes. The distribution of logarithmic reference transmission shows the strokes that are *available* for the selected station to detect. The sub-distribution of logarithmic reference transmission *only for the strokes that are detected by the selected station* shows the relationship between detectability (by the selected station) and logarithmic reference transmission (relative to the selected station). We would expect that if the model has some correlation to observational reality, then the strokes detected by the selected station would be bunched at the high-transmission end of the distribution, and would be sparse or absent in the low-transmission end of the distribution. On the other hand, if the model were basically worthless, then there would be no strong correlation between observed detectability and model-predicted logarithmic reference transmission.

The reader should keep in mind that stations do not all have the same effectiveness in detecting lightning [Hutchins, 2014]. We will call this "sensitivity", but this does not mean something so simple as system gain. Rather, the two most important factors are, first, the level of background VLF noise affecting the selected station, and, second, the abundance of nearby lightning [Hutchins, 2014]. The effect of abundant nearby lightning is to reduce the ability of the station to participate in network detections of distant lightning strokes. This is because each WWLLN station has a software-adjusted trigger threshold for capturing a

pulse to become a candidate for participation in a network location of strokes. The threshold is sluggishly (~ 2 minutes of inertia) adjusted, so as to continuously keep the rate of station triggers not greater than 3 per second. Abundant nearby lightning interacts with this feedback to increase the trigger level and thus reduce the ability of that station to trigger on distant lightning.

4.d2 Ten case studies of patterns of detection/non-detection

Atuona case

Figure 4(a) maps the density of the first cohort of strokes, having mostly-sunlit paths to Atuona. The color scale is *relative to the maximum-density pixel in this plot*, with blue meaning $0.01 \times \text{maximum}$, and red meaning maximum. The resolution is 1-deg X 1-deg. The white areas are $< 0.01 \times \text{maximum}$. The stroke density is displayed only within the -40 to $+40$ deg N band. The curves of $|\text{dip angle}| = 30, 45$ deg are shown in heavy black, while the geomagnetic equator is shown as a thinner black curve. Neither the $|\text{dip angle}|$ curves, nor the stroke density, are shown within the antipodal cone. Also, the -45 deg dip-angle curve is not shown where (southmost South America) it is outside the latitude band.

Figure 4(b) is like Figure 4(a), *except that the density is only for the subset of the day-cohort strokes that are detected by Atuona*. Thus comparison of Figure 4(a, b) gives a visual map of the pattern of day-cohort detection/non-detection by Atuona. Note that the eastern two-thirds of South America's day-cohort lightning is not detected by Atuona, whilst the lightning in SE Asia and Indonesia, though no closer, is largely detected.

Reminder: The color range in the second panel, Figure 4(b), is determined *only* by the densities in Figure 4(b), and is *unrelated* to the color range in the first panel, Figure 4(a). Thus for example, the threshold for blue ($0.01 \times \text{maximum}$) is different (and smaller) in Figure 4(b) than in Figure 4(a). This allows blue cells to appear in the second panel, in principle, at a few locations that are white (sub-blue) in the first panel.

Figure 4(c) maps the value of the day logarithmic reference transmission, for all grid points within the selected latitude band, regardless of the incidence of lightning there. The only exception is that the transmission is whited-out in the antipodal cone. The displayed value is lumped into just four ranges of logarithmic reference transmission: > -2 (red), -2 to -3 (yellow), -3 to -4 (green), and < -4 (blue).

Figures (4d-e) are exactly like Figures 4(a-b) except for the second cohort of strokes, having mostly dark paths to Atuona. Figure 4(f) is like Figure 4(c), except for the *night* logarithmic reference transmission. In night conditions, the asymmetry becomes more dramatic. Atuona detections in South America become insignificant. Comparing Figures 4(c,f), we see that the model prediction is consistent with observations.

Figure 4(g) shows histograms of the actual *instantaneous* logarithmic reference transmission, taking account of the *instantaneous solar zenith angle at each point along the path*. This is not the contrived "day" or "night" prediction of Figures 4 (c,f). The black curve in Figure 4(g) is for all 9.21×10^8 strokes within the latitude band, while the red curve is for only the 1.09×10^8 strokes in that band detected by Atuona. By comparing the two curves, it is apparent that Atuona's detection rate falls off rapidly for logarithmic reference transmission < -2 , and is completely insignificant for < -4 . These are empirical facts based on the distribution of lightning amplitudes, the proximity of the lightning to Atuona, the performance of the network, and the performance of this particular station. The empirical evidence of Figure 4(g) allows us to interpret the model predictions for contrived pure-day (Figure 4c) and contrived pure-night (Figure 4f). The red-shaded regions correspond to logarithmic reference transmission > -2 . We can thus interpret the red regions in Figures 4(c,f) as having unimpeded detectability (at least as far as D-layer effects are concerned.) The yellow-shaded regions are predicted to have relatively lower detection success, though not zero. Green is even lower, and there are predicted to be essentially no detections in the blue-shaded regions, where logarithmic reference transmission is < -4 . With that as a guide, we can now appreciate that the behavior of Figure 4(b), relative to Figure 4(a), is roughly consistent with the contrived day model (Figure 4c) and the empirical distribution (Figure 4g). Similarly, the behavior of Figure 4(e), relative to Figure 4(d), is roughly consistent with the contrived night model (Figure 4f) and the empirical distribution (Figure 4g). Notably,

Atuona’s complete non-detection of any lightning in South America for mostly-dark paths (Figure 4e) is consistent with the all-blue shading of South America (Figure 4f) in the night model. Likewise, Atuona’s strong detection in the Australasia sector for mostly-dark paths (Figure 4e) is consistent with that region’s being shaded red (Figure 4f) in the night model.

The map-based displays (Figures 4a-f) are useful for illustrating the geographic patterns of detection/non-detection by Atuona for two extreme cases, as well as comparing those patterns with the respective model predictions. However, these map-based displays are extremely complicated to follow, and are patchy in their coverage due to the uneven geographical and temporal occurrence of lightning [Christian *et al.*, 2003].

Ultimately, the entire quantitative outcome of our data for Atuona can be distilled into the far simpler and clearer Figure 4(g), which uses *all* the available strokes in the latitude band, without parsing for contrived special cases (mostly-day, mostly-dark). The parent distribution (black curve) shows that $> 50\%$ of the network-detected strokes have logarithmic reference transmission (to Atuona) < -3 , whilst by contrast, for the subset detected by Atuona (red curve) there are very few detected strokes in that range. Thus the predictive model is consistent with the pattern of Atuona’s detection/non-detection. (We take as axiomatic that large signals tend to be easier to detect than are small signals.)

Tahiti case

Tahiti is close to Atuona though at somewhat larger $|\text{dip angle}| \sim 30$ deg. Figure 5 is like Figure 4, but for the Tahiti case. Because Tahiti has operated during almost the entirety of the study epoch, it has more strokes both in the parent distribution (1.94×10^9) and the Tahiti-detected distribution (1.93×10^8) compared to Atuona. The Tahiti detections are almost entirely confined to logarithmic reference transmission (to Tahiti) > -2.5 (Figure 5g), consistent with being a less sensitive station than Atuona. Tahiti almost totally fails to detect lightning in the Americas in night conditions (Figure 5e), while Tahiti is highly successful with the Australasia sector.

Again, as commented earlier in the case of Atuona, all the quantitative evidence is condensed into Figure 5(g); the geographical map presentations are qualitative by comparison. And again, the sharp cut-off of the red curve in Figure 5(g) shows that the model has predictive value for Tahiti detection/non-detection.

Peru case

Figure 6 shows the Peru case. This is the first of our two cases on the west margins of lightning-rich continents. Like Tahiti, Peru can detect almost only for predicted logarithmic reference transmission (to Peru) > -2.5 (Figure 6g). In the daytime case (Figures 6a-c), Peru can detect well throughout South America. In the nighttime case (Figures 6d-e), Peru cannot detect strokes in the eastern half of its own continent, even as it detects in far more distant Micronesia. This is well predicted by Figures 6(c,f). All the quantitative outcomes of the data for Peru are summarized in Figure 6(g), and it indicates the model is consistent with the Peru station’s detection/non-detection. If the model were fundamentally inconsistent with the observations, then the red curve in Figure 6(g) would not be selective for the high-transmission end of the abscissa.

Costa Rica case

Figure 7 shows the Costa Rica case. Costa Rica can detect mostly for predicted logarithmic reference transmission (to Costa Rica) > -2.5 (Figure 7g). During night conditions (Figures 7d-e), Costa Rica loses detection for strokes in much of eastern South America. During those same night conditions, Peru gains detections in the far more distant Australasia and Micronesia sector, where there are few daytime detections (Figures 7a-b). All the quantitative outcomes of the data for Costa Rica are summarized in Figure 7(g), and it indicates the model is consistent with the Peru station’s detection/non-detection.

Belem case

Figure 8 shows the Belem case. One of our least sensitive stations, Belem is essentially unable to detect for strokes whose predicted logarithmic reference transmission (to Belem) < -2.0 (Figure 8g). Some of western

Africa lightning is detected by day, but nothing by night. This is consistent with the day and night model predictions (Figures 8c,f). All the quantitative outcomes of the data for Belem are summarized in Figure 8(g), and it indicates the model is consistent with the Belem station's detection/non-detection.

Dakar case

Figure 9 shows the Dakar case. Like Peru, Dakar lies on the western edge of a lightning-prone continent. Figure 9(g) shows that Dakar cannot detect lightning whose predicted logarithmic reference transmission (to Dakar) < -2.0 . During daytime Dakar can detect strokes in all but the easternmost part of Africa (Figures 9a-b), but during the night, Dakar loses all of Africa coverage save for the western bulge proximal to the station itself (Figures 9d-e). All of these effects are consistent with Figures 9(c,f,g). The model predictions are grossly consistent with the Dakar pattern of detection/non-detection.

Pune case

Figure 10 shows the Pune case. Pune is between the Australasia's and Africa's lightning-prone regions. As seen in Figure 10(g), Pune's detections are almost all for strokes whose predicted logarithmic reference transmission (to Pune) > -2.3 . During nighttime (Figure 10e) but not during daytime (Figure 10b), Pune can detect significant lightning in South America. Similarly, during nighttime (Figure 10e) Pune cannot detect lightning further east than Thailand, while in daytime (Figure 10b), Pune's detection extends further eastward over Borneo. These are predicted by the model in Figures 10(c,f,g). The model predictions are consistent with the pattern of Pune detections/non-detections.

Singapore case

Figure 11 shows the Singapore case. Similar to Pune, Singapore detections are mostly confined to strokes whose predicted logarithmic reference transmission (to Singapore) > -2.3 (Figure 11g). The geographical patterns for the night cohort of strokes show extreme asymmetry favoring strokes on the West of the station and disfavoring strokes on the East of the station. The pattern of detection/non-detection by Singapore is grossly consistent with the model predictions (Figures 11 c,f,g).

Honolulu case

We complete this survey with two cases where the selected station is at higher magnetic latitude than so far. Figure 12 shows the Honolulu case. The bulk of Honolulu's detections are for strokes whose predicted logarithmic reference transmission (to Honolulu) > -2.5 (Figure 12g), with a low tail out to -4 , as had been the case with Atuona. For the nighttime cohort of strokes (Figures 12d,e), Honolulu detects very few strokes in South America, whilst its more distant detections on the West go all the way across India. The Honolulu patterns of detection/non-detection are grossly consistent with the model predictions (Figures 12c,f,g).

Tel Aviv case

Finally, Figure 13 shows the Tel Aviv case, located at dip angle > 45 deg. Virtually all of Tel Aviv's detections are for strokes whose predicted logarithmic reference transmission (to Tel Aviv) are > -2.5 (Figure 13g). Despite its relatively high magnetic latitude, long range detection eastward or westward into the low magnetic latitudes still displays the asymmetry favoring strokes from South America over strokes in Australasia, particularly for the night cohort (Figure 13e). The Tel Aviv pattern of detection/non-detection is grossly consistent with the model predictions (Figures 13c,f,g).

4e. Closing the observational case that the model is consistent with the data

We have presented observations of the geographical patterns of detection/non-detection for ten selected stations around the globe, at low and low-middle latitudes. The geographical patterns are shown for separately for mostly-day, and then mostly-night transmission paths. The observed patterns of detection/non-detection are consistent with the patterns of predicted logarithmic reference transmission, for the respective day or night cases. More quantitatively, the distributions of actual logarithmic reference transmission to each selected station, both for the parent distribution and for the subset of strokes in whose location the selected

station is a participant (i.e. detected by the selected station), show that the paths for *detected* strokes are clustered at the high-transmission end of the parent distribution. Thus the model predicts which cases are more likely to be detected, and which are not.

As mentioned earlier, this logic rests on an axiom: All other things being equal, a strong pulse is more likely to be detected than is a weak pulse. And we assume, all other things being equal, that paths involving relatively weaker transmission will cause weaker detected pulses than will paths involving relatively stronger transmission.

We now perform a "sanity check" on this key assumption. Figure 14 shows distributions of the detected, raw ADC amplitudes for pulses detected by the Tel Aviv station. The ADC is 16-bits deep (0 to 65535), but we show the distributions out to only ADC level 5000. The two panels in Figure 14 are for two adjacent tranches of modeled logarithmic reference transmission: (a) > -2 , and (b) in the range -2 down to -2.5 . The shoulder at about ADC level 100 - 200 corresponds to the local-time servo adjustments of the station's software trigger threshold. The higher-transmission distribution (a) contains 1.8×10^8 detections, while the lower-transmission distribution (b) contains only $\sim 12\%$ as many detections. Moreover, in (a) the high-transmission distribution's tail, relative to the distribution's peak, is much more relatively populated than in (b). Finally, whereas in (a) the peak occurs at ADC level ~ 800 , in (b) it has retracted to ~ 500 .

Thus Figure 14 supports the picture that the high-transmission population's extended tail (to higher values of detected ADC level) becomes depleted at lower transmission, with those tail members being swept to the left end of the distribution. Most of those then are swept to sub-threshold ADC level, but some remain above the threshold and constitute the peak in (b). Let us see if this picture makes quantitative sense. The change in logarithmic reference transmission between these two tranches is in the range 0.5 to 0.75, depending on where, within a tranche, it is figured. The first part of this study demonstrated that the "r" parameter, which multiplies the logarithmic reference transmission to give the actual physical transmission, was fitted by the data of JHB1 to lie in the range from 2 to 3 Nepers (see Figures 6 and 9, and discussion thereof, in JHB1). Let us choose 2.5 Nepers. Then the change in logarithmic reference transmission between these two tranches in the range 0.5 to 0.75 Nepers corresponds to a change in *physical* logarithmic transmission in the range 1.25 to 1.88 Nepers. In linear amplitudes, the range is a multiplicative factor from ~ 3.5 to ~ 6.5 . This implies that the transition from Figure 14(a) to 14(b) can be understood as taking tail members in (a) and moving them leftward (to lower ADC level) in (b) down to ADC levels only $1/3.5$ to $1/6.5$ as big. Fortunately, we see that the tail in (a) contains sufficient population to permit this simple occur. Thus the relative distributions of detected raw ADC levels are consistent with the predicted transmissions of adjacent tranches of the transmission distribution.

5. Conclusions

This is the second part of a two-part study of broadband VLF propagation from lightning strokes to WWLLN stations. The first part of the study (JHB1) had developed a model for the effects of the ionospheric D-layer on long-range VLF transmission in the Earth-Ionosphere Waveguide. The model makes the counter-intuitive prediction that, for dip angles in the range -30 to $+30$ deg, propagation toward the west half of magnetic azimuths will be dramatically worse during conditions of darkness (along the propagation path) than during conditions of daylight. This feature had never been remarked before in the literature, although it is in fact also embedded in the standard LWPC code. We surmise that the reason the feature had never been remarked is that the LWPC is an end-to-end treatment that tends to obscure, to the code's user, the details of differential transmission at any one point on the propagation path.

Our model had been applied in JHB1 to explaining the inter-station ratios of signal amplitudes from the same stroke at different stations. That approach, in common with all virtually all other approaches done by prior workers, was based on the measurement of VLF amplitudes. However, we found that the amplitude-based method was inadequate to the test the model's counter-intuitive prediction regarding the day/night control of westerly propagation. That is because the amplitude-based approaches require detections in order for amplitudes to be determined. "No detections, no amplitudes".

This second part of the study circumvents that problem by adopting an opposite approach. Rather than use received signal amplitudes as the raw data, we now use the observed statistical patterns of detection/non-detection. We compare those patterns to our model's predictions of the D-layer contributions to path transmission. By focusing on the variations between daylit and dark conditions, we also avoid the confounding effect of ground losses, as the latter are invariant between daylit and dark conditions.

We highlight the geographical patterns of detection/non-detection from each of ten selected stations arranged around diverse longitudes. For each of these stations, we identify strokes whose paths are either mostly daylit or mostly dark. The patterns of detection/non-detection in these two special cases are then compared with the predictions of our transmission model, for either all-lit paths or all-dark paths respectively. The spatial agreement between observation and model is good. We then use *all* the strokes, not just those whose paths are mostly lit or mostly dark, and calculate the modeled logarithmic reference transmission along each stroke's path to the selected station, taking account of the instantaneous solar zenith angle at each point along the path. We tally the distribution of logarithmic reference transmission, both for the parent population of strokes, and for the subset of strokes that are detected by the selected station. We find consistently, for all of our ten selected stations, that the detected subset's distribution of logarithmic reference transmission is entirely crowded to the high-transmission end. This suggests that the model's predictions of transmission are pertinent.

Finally, and most importantly, our ten case studies robustly demonstrate that for dip angles in the range -30 to +30 deg, during conditions of darkness there is dramatically worse transmission from magnetic East to West than from magnetic West to East, whereas for daylit conditions, this is much less pronounced. These findings are operationally significant for long-range lightning detection. For example, WWLLN's Pacific stations Atuona, Tahiti, and Honolulu are not able in dark-path conditions to contribute significantly to locating lightning in South America, though they are extremely useful over comparable distances with lightning in Australasia. Similarly, under dark-path conditions, Peru basically misses the eastern half of its own continent, and Dakar sees even less of its own continent. For the same reason, during dark-path conditions, Pune is very good for detecting lightning in Africa but misses almost all lightning at similar distances in Australasia. These effects are not subtle, when viewed geographically in terms of areas of detection and non-detection.

Acknowledgements

The authors are using data from the World Wide Lightning Location Network, a collaborative consortium of over seventy worldwide collaborators, managed at the University of Washington. The data would not exist but for the cooperative efforts of all of WWLLN's participants. For sale to researchers who are not WWLLN participants, WWLLN data are available, at a nominal price to cover overhead costs of running the network, and archiving / distributing the data. To find out about such data access, see <http://wwlln.net/>

References

- Barber, N. F., and D. D. Crombie (1959), V. L. F. reflections from the ionosphere in the presence of a transverse magnetic field, *Journal of Atmospheric and Terrestrial Physics* , 16 , 37-45.
- Bickel, J. E., J. A. Ferguson, and G. V. Stanley (1970), Experimental observation of magnetic field effects on VLF propagation at night, *Radio Sci.* , 5 (1), 19-25.
- Budden, K. G. (1985), *The Propagation of Radio Waves* , 669 pp., Cambridge University Press, Cambridge.
- Chand, A. E., and S. Kumar (2017), VLF modal interference distance and nighttime D region VLF reflection height for west-east and east-west propagation paths to Fiji, *Radio Science* , 52 , 1004-1015, doi:10.1002/2016RS006221.
- Christian, H. J., et al. (2003), Global frequency and distribution of lightning as observed from space by the Optical Transient Detector, *J. Geophys. Res.* , 108 (D1), 4005, doi:10.1029/2002JD002347, doi:10.1029/2002JD002347.

- Crombie, D. D. (1958), Differences between the east-west and west-east propagation of VLF signals over long distances, *Journal of Atmospheric and Terrestrial Physics* , *12* (2-3), 110-117.
- Crombie, D. D. (1966), Further Observations of Sunrise and Sunset Fading of Very-Low-Frequency, *Radio Science* , *1* , 47-51, doi:10.1002/rds19661147.
- Cummer, S. A. (2000), Modeling electromagnetic propagation in the Earth-ionosphere waveguide, *IEEE Trans. Antennas Propag.* , *48* (9), 1420-1429.
- Hutchins, M. L. (2014), Source, propagation, and effects of lightning in the Earth-ionosphere system, PhD thesis, 156 pp, University of Washington.
- Hutchins, M. L., R. H. Holzworth, C. J. Rodger, and J. B. Brundell (2012), Far-field power of lightning strokes as measured by the World Wide Lightning Location Network, *J. Atmos. Oceanic Technol.* , *29* , doi:10.1175/JTECH-D-11-00174, 1102-1110, doi:10.1175/JTECH-D-11-00174.
- Hutchins, M. L., A. R. Jacobson, R. H. Holzworth, and J. B. Brundell (2013), Azimuthal dependence of VLF propagation, *J. Geophys. Res.* , *118* , 1-5, doi:10.1002/jgra.50533, doi:10.1002/jgra.50533.
- Jacobson, A. R., R. Holzworth, and X.-M. Shao (2010), Full-wave reflection of lightning long-wave radio pulses from the ionospheric D-region: Comparison with midday observations of broadband lightning signals, *J. Geophys. Res. -Space* , *115* , A00E27, doi:10.1029/2009JA014540, doi:10.1029/2009JA014540.
- Jacobson, A. R., R. H. Holzworth, and J. B. Brundell (2021), Using the World Wide Lightning Location Network (WWLLN) to Study Very Low Frequency Transmission in the Earth-Ionosphere Waveguide: 1. Comparison with a Full-Wave Model, *Radio Science* , *56* , doi:10.1029/2021RS007293.
- Jacobson, A. R., X. Shao, and R. H. Holzworth (2009), Full-wave reflection of lightning long-wave radio pulses from the ionospheric D-region: Numerical model, *J. Geophys. Res. - Space* , *114* , A03303, doi:10.1029/2008JA013642, doi:10.1029/2008JA013642.
- Jacobson, A. R., X.-M. Shao, and E. Lay (2012), Time-domain waveform, and azimuth variation, of ionospherically reflected VLF/LF radio emissions from lightning, *Radio Sci.* , *47* , RS4001, doi:10.1029/2012RS004980.
- Pappert, R. A., and J. A. Ferguson (1986), VLF/LF mode conversion model calculations for air to air transmissions in the Earth-ionosphere waveguide, *Radio Sci.* , *21* , 551-558.
- Pappert, R. A., and L. R. Hitney (1988), Empirical modeling of nighttime easterly and westerly VLF propagation in the Earth-ionosphere waveguide, *Radio Sci.* , *23* (4), 599-611.
- Piggott, W. R., M. L. V. Pitteway, and E. V. Thrane (1965), The numerical calculation of wave-fields, reflexion coefficients and polarizations for long radio waves in the lower ionosphere. II, *Phil. Trans. Roy. Soc. Lon.* , *257* (1079), 243-271.
- Pitteway, M. L. V. (1965), The numerical calculation of wave-fields, reflexion coefficients and polarizations for long radio waves in the lower ionosphere. I, *Phil. Trans. Roy. Soc. Lon.* , *257* (1079), 219-241.
- Samane, J. E., J.-P. Raulin, E. L. Macotela, and W. R. G. Day (2015), Estimating the VLF modal interference distance using the South America VLF Network (SAVNET), *Radio Science* , *50* , 122-129, doi:10.1002/2014RS005582.
- Taylor, W. L. (1960), VLF attenuation for East-West and West-East daytime propagation using atmospheric, *Journal of Geophysical Research* , *65* (7), 1933-1938.
- V-MOD, I. W. G. (2010), International Geomagnetic Reference Field: the eleventh generation, *Geophys. J. International* , *183* (3), 1216-1230, doi:10.1111/j.1365-246X.2010.04804.x.
- Volland, H. (Ed.) (1995), *Handbook of atmospheric electrodynamics* , CRC Press, Boca Raton, Florida, USA.

Wait, J. R., and K. Spies (1960), Influence of Earth curvature and the terrestrial magnetic field on VLF propagation, *Journal of Geophysical Research* , 65 (8), 2325-2331.

Wait, J. R., and K. P. Spies (1964), NBS Technical Note 300: Characteristics of the Earth-ionosphere waveguide for VLF radio waves, edited by U. S. D. o. C. National Bureau of Standards (now National Institute of Standards and Technology, NBS.

Yabroff, I. W. (1957), Reflection at a Sharply-Bounded Ionosphere, *Proc. Inst. Radio Engrs.* , 45 , 750-753.

Figure captions

Figure 1: Model amplitude reflectivity (vertical axis) vs propagation magnetic azimuth (horizontal axis). Color marks magnetic dip angle, from 5 deg (blue) to 85 deg (red). Curve for dip angle = 45 deg is dashed. Model assumes angle-of-incidence is 85 deg, and is averaged over the band 5 - 20 kHz. (a) Day case. (b) Night case, with labels on curves for dip angle = 30, 45 deg. The horizontal black line on both panels is through the minimum of the curve for dip angle = 45. deg in (b). See Table 1 for parameter values.

Figure 2: Comparison of Atuona detection efficiency against strokes in two roughly equidistant geographic boxes. (a) Showing the East box, over northwestern South America. (b) For all strokes in East box, showing the distribution of fraction of instantaneous path (to Atuona) that is daylit. This includes all strokes in the East box, not just those detected by Atuona. Horizontal resolution is 0.01. (c) Detection efficiency (DE) of Atuona against strokes in East box, as a function of the instantaneous daylit fraction of the path. (d) Showing the West box. (e) For all strokes in West box, showing the distribution of fraction of instantaneous path (to Atuona) that is daylit. (f) Detection efficiency (DE) of Atuona against strokes in West box, as a function of the instantaneous daylit fraction of the path. Note the order-of-magnitude difference in DE scales between (c) East and (f) West boxes.

Figure 3: Geomagnetic setting of each of the ten selected stations. Each station is shown as a rectangle, either white or black so as to contrast with the background. The color shading of the background is magnitude of dip angle, from 0 (black) to 74 deg (red). Only (i) has a different color scale: 0 (black) to 76 deg (red). The colors are shown within latitude bands -40 to +40 deg, except -30 to +50 deg for (i) Honolulu. Also, discrete curves are drawn, where dip angle = -30, -45, +30, and +45 deg. The white cone at each station's antipode is excluded from the analyses, because the Great Circle Paths from strokes within those cones extend poleward of +/- 55 deg latitude.

Figure 4: Patterns of detection/non-detection for Atuona. (a) Spatial density of WWLLN-located strokes within the latitude band for which the Great Circle Path is > 80% sunlit. The maximum for this density is red, while blue is 1% of the maximum. White areas outside of the antipodal cone correspond to stroke density less than 1% of the maximum. The discrete lines are at dip angle = 0, +/- 30, and +/- 45 deg. Neither the stroke density, nor the curves, are shown within the antipodal cone or outside of the latitude band. (b) Spatial density of the subset of strokes in whose location Atuona participates, for which the Great Circle Path is > 80% sunlit. The new maximum is shown as red, and 1% of this new maximum is shown as blue. (c) Day model logarithmic reference transmission (see text) versus position, in four ranges: > -2 (red), from -2 to -3 (yellow), from -3 to -4 (green), and < -4 (blue). Model is not shown within the antipodal cone or outside of the latitude band. (d) Similar to (a) but for Great Circle Paths < 20% sunlit. (e) Similar to (b) but for Great Circle Paths < 20% sunlit. (f) Similar to (c) but for night model. (g) Histogram of logarithmic reference transmission. Black curve: all strokes in latitude band excluding antipodal cone. Red curve: only those strokes in whose location Atuona participates.

Figure 5: Similar to Figure 4, but for Tahiti station.

Figure 6: Similar to Figure 4, but for Peru station.

Figure 7: Similar to Figure 4, but for Costa Rica station.

Figure 8: Similar to Figure 4, but for Belem station.

Figure 9: Similar to Figure 4, but for Dakar station.

Figure 10: Similar to Figure 4, but for Pune station.

Figure 11: Similar to Figure 4, but for Singapore station.

Figure 12: Similar to Figure 4, but for Honolulu station. Note that latitude band is -30 to +50 deg, for this station only.

Figure 13: Similar to Figure 4, but for Tel Aviv station.

Figure 14: Distribution of raw amplitude (ADC level) for WWLLN-located strokes detected by Tel Aviv station. (a) For logarithmic reference transmission > -2.0 . (b) For logarithmic reference transmission from -2.0 to -2.5.

1 **Using the World Wide Lightning Location Network**
2 **(WWLLN) to study Very Low Frequency transmission in**
3 **the Earth-Ionosphere Waveguide: 2. Model test by patterns**
4 **of detection/non-detection**

5
6 **Abram R. Jacobson¹ and Robert H. Holzworth**
7 Earth and Space Sciences Dept., University of Washington, Seattle U. S.

8
9 and

10
11 **James B. Brundell**
12 Physics Dept., University of Otago, Dunedin NZ

13
14
15 1: Corresponding author Abram R. Jacobson, abramj@uw.edu

16
17
18

19 **Abstract**

20

21 This is the second half of a two-part study. In the first part, we had used the World Wide
22 Lightning Location Network's recorded signal amplitudes to test a model of Very Low
23 Frequency signal transmission from the lightning to each sensor. The model predicts a dramatic
24 worsening of transmission at low magnetic latitudes, for nighttime propagation (compared to
25 daytime propagation) toward magnetic West. However, we found that the use of amplitudes was
26 ill-adapted for testing the model under conditions of a deep outage of transmission. Since the
27 relative weakening of nighttime transmission is rather counter-intuitive, we have now developed
28 an alternative approach to testing that model prediction. This alternative approach highlights the
29 patterns of detection/non-detection of several low-magnetic-latitude WWLLN stations and
30 compares those patterns with the appropriate patterns of the model transmission.

31 1. Introduction

32

33 This is not a new topic. East-west asymmetry in VLF (Very Low Frequency; 3-30 kHz)
34 propagation in the Earth-Ionosphere Waveguide had been inferred as early as the 1920's [see the
35 historical review by *Crombie*, 1958]. The geomagnetic control over VLF propagation is expected
36 to depend strongly on two orientational parameters [*Budden*, 1985; *Piggott et al.*, 1965;
37 *Pitteway*, 1965; *Wait and Spies*, 1960; *Wait and Spies*, 1964; *Yabroff*, 1957]. One is the dip angle
38 of the geomagnetic field, and the other is the propagation magnetic azimuth of the VLF
39 wavefield. Along any long-range propagation Great Circle Path, both of these orientational
40 parameters can widely vary. Thus, e.g., it is only very approximate to characterize the
41 propagation magnetic azimuth "of the path" by its value at a path endpoint. The research results
42 we review below can be broadly separated as to whether they just grossly consider the whole
43 path together, or whether they dissect the path into small segments and use a different
44 propagation azimuth and magnetic dip within each segment. The former we will call "bucket"
45 approaches, in that they just characterize the entire path as being effectively at one propagation
46 magnetic azimuth. By contrast, the model comparisons which consider the local nature of the
47 two orientational parameters will be called "local" approaches.

48

49 All studies of the azimuthal asymmetry of VLF propagation prior to the present have been based
50 on observing the effect of magnetic propagation azimuth on received amplitudes. This is equally
51 true when the signals received were from narrow-band artificial beacons [e.g., *Bickel et al.*,
52 1970; *Pappert and Hitney*, 1988] or when derived from lightning strokes [e.g., *Hutchins et al.*,
53 2013; *Jacobson et al.*, 2021; *Taylor*, 1960]. In the already-published [*Jacobson et al.*, 2021] first
54 half of the present study, henceforth referred to as "JHB1", we followed the amplitude-
55 comparison approach. However, we reached a cul-de-sac with that approach, when we tried to
56 test a particular non-intuitive though impactful prediction of our model [*Jacobson et al.*, 2010;
57 *Jacobson et al.*, 2009; *Jacobson et al.*, 2012]. The prediction is that for propagation at low dip
58 angle, e.g. in the range -30 to +30 deg, propagation toward the magnetic West is deeply
59 attenuated during dark-path conditions (night), *relative to sunlit-path (day) conditions*.
60 Curiously, this counter-intuitive effect had not been overtly remarked prior to JHB1, though the
61 physics package of the comprehensive, state-of-the-art path simulator, LWPC [*Pappert and*
62 *Ferguson*, 1986], certainly contains all the relevant physics.

63

64 We found in JHB1 that the sought-after dark-path conditions apparently caused such a dearth of
65 numerically sufficient lightning detections at the pertinent stations, so that amplitudes could not
66 be determined with statistical accuracy. Thus JHB1 could not test its most interesting model
67 prediction. "No detection, no amplitude".

68

69 This shortcoming of JHB1 motivated the present study, which is the second part of the study
70 begun by JHB1. We completely change strategy in this paper. Rather than comparing
71 amplitudes, we examine observed statistical patterns of detection/non-detection from ten selected
72 stations. We compare those patterns to predictions of the model. The stations are chosen to
73 represent all longitude sectors and all Universal Times, and to include many diverse paths from
74 the lightning locations to the stations, in such a manner as to provide compelling statistical
75 evidence on the model's predictions. The number of paths included exceeds 15-billion. Each of
76 these paths is then dissected into 50 path segments, for a grand total exceeding 750-billion path

77 segments. At each path segment, the geomagnetic dip angle and magnetic propagation azimuth
78 are calculated, along with the instantaneous solar zenith angle, are combined to predict the
79 modeled contribution of that path segment to the overall integrated attenuation for that path.
80

81 **2. Background**

82 **2a. Prior observations of east-west asymmetry of VLF propagation**

83 Here we review the carefully documented work that began in the 1950's. Crombie described new
84 measurements performed in New Zealand during 1957 [*Crombie, 1958*], one purpose of which
85 was to investigate the asymmetry earlier hinted at by the scattered results of the 1920's. The
86 16.6-kHz signal from a powerful transmitter ("GBR") in Rugby, UK was received by a magnetic
87 loop and a vertical aerial at Wellington, NZ. The receiver and the transmitter were nearly
88 antipodal. By rotating the loop antenna, Crombie was able to select separately the signal arriving
89 on either Great Circle Path, from respectively NNW or SSE (reckoned at Wellington.) The signal
90 strength on each orientation of the loop was measured versus time during three multi-day
91 periods. The results confirmed not only that the signal arriving from the NNW had 10-15 dB
92 stronger amplitudes than the path arriving from the SSE, but also that the diurnal variations were
93 dissimilar between the two paths. Crombie attributed this difference to the east-west components
94 of each path, although this was left notional. The detailed variation of the magnetic azimuth
95 along each path was not presented or addressed, so that Crombie's work was in the "bucket"
96 category. The diurnal variation was not explained, but the gross difference between eastward and
97 westward propagation was noted.
98

99
100 Shortly after the work by Crombie, there was a systematic attempt to use geolocated lightning to
101 observe the zonal asymmetry of long-range broadband VLF propagation [*Taylor, 1960*].
102 Whereas Crombie had relied on a discrete, narrow-band, man-made beacon, Taylor exploited the
103 powerful broadband emissions of lightning return strokes. Attention was focused on daytime
104 conditions, with most of the paths over seawater. VLF receiver stations in the western United
105 States and in Hawaii, triggering off common lightning strokes, were used to crudely geolocate
106 the lightning, at least within <10% of the path length, by triangulating the direction found at each
107 station. Each station measured and recorded the vertical electric field with a vertical mast, and
108 also provided the direction of arrival from comparing signals on two vertical-magnetic-loop
109 antennas. As was necessary in that era, data were recorded for off-line analysis using
110 oscilloscopes and cameras. The east-to-west attenuation from twenty lightning discharges was
111 used to determine a mean spectral attenuation (dB/1000km) for that direction of propagation.
112 The spectral attenuation was determined for the entire VLF band. Similarly, the spectral
113 attenuation for west-to-east attenuation was determined using sixteen lightning discharges. All
114 observations were for entirely-daylit paths. It was found that attenuation east-to-west exceeded
115 attenuation west-to-east, by approximately 3 dB/1000km for $f < 8$ kHz and by approximately 1
116 dB/1000km for $f > 10$ kHz.
117

118 Taylor's characterization of the paths as "east to west" versus "west to east" [*Taylor, 1960*] is in
119 the bucket category. Moreover Taylor did not consider the control by geomagnetic dip angle;
120 rather, all the paths were simply tagged as "east to west" or as "west to east", regardless of
121 magnetic dip, and then simply labeled with one orientation. The lightning locations are not given

122 [Taylor, 1960], so it would not be possible to retrospectively model Taylor's observations with a
123 more local approach.

124
125 In 1969, the United States Naval Ocean Systems Center conducted airborne measurements of
126 VLF beacon signals on Great Circle Paths from the island of Hawaii toward San Diego and from
127 the island of Hawaii toward Wake. The paths were, respectively, west-to-east and east-to-west
128 paths, entirely over seawater, and entirely nighttime. These data were later presented and
129 compared [Pappert and Hitney, 1988] to state-of-the-art, full-wave waveguide propagation
130 calculations using the LWPC [Pappert and Ferguson, 1986]. The fixed frequencies of the
131 beacons at Hawaii were discretely between 10.9 kHz (the lowest) and 28.0 kHz (the highest).
132 The airborne receiver recorded signal amplitudes due to the multifrequency sounder for the first
133 ~4000 km of each path. Thus the measurements were all done within 4000 km of Hawaii. The
134 VLF data were compared to a model that included detailed tracking of the propagation azimuth
135 and the magnetic dip angle locally at all points along the propagation path. This was a local
136 approach, and was a critical advance over the bucket approach. It was found that the eastbound
137 (San Diego path) signal was very reproducible day-to-day, and was essentially perfectly modeled
138 by LWPC with a generic nighttime profile [Pappert and Hitney, 1988]. The westbound (Wake
139 path) signal, by contrast, was more variable day-to-day, and this adversely affected the
140 agreement with the model, although on average the agreement was satisfactory. The variability
141 for westbound propagation was speculated to be related to sporadic electron-density features near
142 altitude 90 km. We note that the sampled paths did not delve lower than about 30 deg in dip
143 angle.

144
145 In addition to the airborne measurements using the multifrequency beacon, the same aircraft was
146 also deployed to measure the signal from the unique 23.4-kHz signal "NPM" radiated from the
147 area of Honolulu, Hawaii with much higher power than the research multifrequency beacon. The
148 NPM signal was measured along Great Circle Paths from NPM toward Seattle, Ontario
149 (California), Samoa, and Wake Island. Results were reported [Bickel et al., 1970], similarly, out
150 to ~4000 km range, and were entirely over seawater and at night. The authors [Bickel et al.,
151 1970] used an early predecessor of LWPC to compare with waveguide theory, and found that the
152 model predictions of dependence on magnetic azimuth and magnetic dip angle were robustly
153 confirmed at 23.4 kHz by the airborne measurements. Their model comparison was a local
154 approach, exactly similar to that used for the multifrequency beacon data [Pappert and Hitney,
155 1988].

156
157 A more recent entry into the observation of propagation magnetic-azimuth asymmetry was done
158 with the World Wide Lightning Location Network, or WWLLN [Hutchins et al., 2013]. It dealt
159 with over-seawater paths in the Pacific sector, using WWLLN stations at island locations Suva,
160 Tahiti, and Honolulu. This study is in the "bucket" category. The study used lightning strokes
161 jointly detected by all three of those stations (along with other stations as well.) Each lightning
162 stroke's radiated VLF energy was determined with the WWLLN energy retrieval described
163 elsewhere [Hutchins et al., 2012]. The candidate strokes were selected according to the following
164 strict limiting criteria:

165 (a) The WWLLN VLF energy determination for the stroke needed to have an estimated error less
166 than 10% of the VLF energy.

167 (b) The stations participating in the location/energy determination needed to be equally
168 distributed east/west of the stroke location, to within 25%.
169 (c) The strokes were limited to those for which the three paths to Suva, Tahiti, and Honolulu
170 were *all* either less than 5% daylit *or* more than 95% daylit.

171
172 The strokes were selected from those occurring from May 2009 to May 2013. With these criteria,
173 only 0.2% of the stroke population was accepted, that is, only 2×10^6 strokes were accepted.

174
175 The high-confidence energy retrievals for the 2×10^6 accepted strokes allowed each of these
176 stroke's "normalized electric field" to be derived for each stroke, so as to use all the strokes
177 despite their widely differing stroke VLF energies [Hutchins *et al.*, 2013]. The normalization was
178 the rms measured electric field (in units of μVm^{-1}) divided by the square root of the retrieved
179 VLF energy (in units of J). This normalization was tabulated for each of the strokes as the
180 electric field in dB above $1 \mu\text{Vm}^{-1}\text{J}^{-1/2}$.

181
182 The 2×10^6 accepted strokes were grouped into azimuth/distance bins, with eight azimuth bins,
183 each 45 deg wide, and distance bins 500 km wide. The azimuth was the average magnetic
184 azimuth over the path, which is approximate, as the azimuth actually varies along each path.
185 Within each bin, the bin median was used to show variations versus distance and azimuth. In
186 order to highlight azimuthal variation, each attenuation rate was normalized by an "all-azimuth"
187 average. Thus the normalized-attenuation data vary azimuthally with a mean of unity. The
188 normalized-attenuation data were compared to the standard theory of idealized sharp-boundary
189 reflection from a magnetized D-layer [Wait and Spies, 1960]. The agreement between the
190 WWLLN results and the sharp-boundary model was rather good [see Figure 5 in Hutchins *et al.*,
191 2013]. In part this agreement may be fortuitous. The model uses simply a sharp-boundary
192 ionosphere, which is a problem. Moreover, the model did not explicitly treat "day" or "night",
193 but rather tried two electron densities. However, the cited model stuck with $2 \times 10^7 \text{ s}^{-1}$ as the fixed
194 collision electron-neutral rate in the case of either of those electron densities, so they really do
195 not illuminate the difference between night and day reflection conditions. Another cause for
196 caution at the good agreement between the model and the data is that the model was for dip angle
197 of 0 deg, whilst the range of dip-angle magnitude in the paths in the WWLLN study was 0 deg to
198 ~ 45 deg. Therefore it is not ruled-out that the good agreement of the Wait model and the
199 WWLLN data may have been partially fortuitous.

200
201 The legacy results cited above concern direct measurements of the VLF amplitude. We now
202 mention a different set of observations in which east-west asymmetry, or "non-reciprocity", was
203 revealed: The several observations of VLF modal interference for narrow-band transmissions.
204 Here for brevity we mention only a few of these reports, because our case (broadband emissions
205 from lightning) has wide enough bandwidth to essentially wash-out any mode-interference
206 effects. WWLLN's passband of useful VLF energy is roughly 5-20 kHz [see, e.g., Figure 2.2 in
207 Hutchins, 2014]. This mixes interferences of different spatial scale, so that the net result is
208 washed-out.

209
210 An early series of measurements on modal interference [Crombie, 1966] documented markedly
211 different modal-interference wavelengths for several discrete frequencies from 18 to 24 kHz. A
212 more recent study [Samanes *et al.*, 2015] lacked westward paths and thus could not address this

213 non-reciprocity issue. An even more recent study [*Chand and Kumar, 2017*] did not yield
214 unambiguous results on non-reciprocity.

215

216 **2b. Prior modeling of east-west asymmetry of VLF propagation**

217 The reflection of radio waves from the underside of the ionosphere became an active area of
218 research during the 1950s [see the historical references given by, e.g., *Barber and Crombie,*
219 *1959; Wait and Spies, 1960; Wait and Spies, 1964; Yabroff, 1957*]. The problem was nontrivial
220 due to the anisotropy of the dielectric, associated with the gyration of charged particles about the
221 geomagnetic field. This was especially true for VLF waves, whose height of reflection occurs in
222 the lowermost ionosphere, namely the D-layer. The strong electron-neutral collision rate in the
223 D-layer further complicates models of VLF reflection. The models needed to address practical
224 challenges, e.g.:

225 (a) What is the VLF reflectivity?

226 (b) How does it depend on solar zenith angle?

227 (c) How does the reflectivity depend on angle-of-incidence?

228 (d) How does the reflectivity depend on local propagation magnetic azimuth (reckoned
229 clockwise from local magnetic North) and on local magnetic declination ("dip angle")?

230 (e) How does the reflectivity depend on electron-neutral collision rate?

231

232 Starting late in the 1950's, sharp-boundary treatments of the collisional, anisotropic VLF
233 reflection process were set up analytically and solved numerically with newly available digital
234 computers [*Barber and Crombie, 1959; Wait and Spies, 1960; Wait and Spies, 1964; Yabroff,*
235 *1957*]. The first numerical model of an arbitrarily-layered (rather than just a sharp boundary) D-
236 layer [*Piggott et al., 1965; Pitteway, 1965*] followed quickly, although its physical implications
237 appear to have been only slowly appreciated. The Pitteway model for the continuously varying
238 D-layer solved the Maxwell Equations for the altitude-dependent, anisotropic, and complex
239 susceptibility tensor. All of the sharp-boundary models, as well as the Pitteway model, dealt with
240 the elementary reflection of an incident plane wave.

241

242 Such plane-wave models are excellent for providing insights on "process" questions, such as
243 those cited in the previous paragraph. However, for long-range "multi-hop" propagation, it is
244 more efficient, though less heuristically instructive, to cast the problem in terms of waveguide
245 modes in the spherical-shell Earth-ionosphere waveguide (EIWG). The modes are akin to
246 cylindrical waves from a point source within a parallel-plane waveguide, except that the
247 waveguide elements are (approximately) *concentric spherical surfaces* [see the illuminating
248 tutorial by *Cummer, 2000*]. A waveguide model provides a point-to-point complete description
249 of the VLF transmission along any given Great Circle path. This includes all portions of the path.
250 The first portion consists of 3-dimensional expansion of the wavefield into a hemisphere. The
251 next portion takes account of the first ionospheric reflection, which effectively is a transition to
252 spherical-shell EIWG propagation. This transition needs many higher-order modes to describe
253 the wavefield, because at such a short range (e.g., < 1000 km) a broad range of plane-wave
254 "angles of incidence" are at play [*Cummer, 2000*]. Ultimately, however, at longer range the
255 waveguide modes simplify. For a vertical-dipole source near ground level, and a vertical-dipole
256 receiver also near ground level, the modes simplify at large distances to the fundamental
257 Transverse Magnetic (TM) mode. Thus the transmission characteristics vary from 3-dimensional
258 expansion into a hemisphere, to a single 2-D, fundamental TM mode in the waveguide.

259
260 The waveguide approach was perfected in the Long Range Propagation Capability, or LWPC
261 [Pappert and Ferguson, 1986] suite of computer codes developed by the United States Navy.
262 The LWPC includes an atlas of Earth-surface conductivity. The user can select a D-layer model,
263 usually exponential profiles of electron density and of electron-neutral collision rate. The LWPC
264 contains "everything" in one master code suite. LWPC uses just an approximation of the D-layer
265 electron-density profile, but that is justified by the impossibility of knowing any better profile at
266 any given instant.

267
268 One adverse side-effect of its end-to-end completeness is that the LWPC blurs (to the LWPC
269 user) the role of *local* parameters, such as solar magnetic propagation azimuth and local
270 magnetic dip angle. These vary along the path, but the LWPC's end-to-end approach path-
271 integrates over their local variations, and all the user sees is the result of the path integration.
272 Thus, despite its completeness, premiere accuracy, and reliability, the LWPC is not
273 pedagogically illuminating for exploring individual local *processes* in isolation.

274
275

276 3. Recap of part 1 of the present study

277

278 3a. Plane-wave reflectivity and path transmission

279 This article is part 2 of a two-part study; here, we briefly recap the results of the first part, from
280 JHB1. The work to follow entirely depends on JHB1, and the reader should refer to that
281 published article for details beyond the brief recap here.

282

283 We rely on a numerical model of plane-wave reflection from a diffuse, collisional, anisotropic D-
284 layer [Jacobson *et al.*, 2010; Jacobson *et al.*, 2009; Jacobson *et al.*, 2012]. Our model is a
285 modernization of Pitteway's groundbreaking treatment [Piggott *et al.*, 1965; Pitteway, 1965]. We
286 represent the electron-neutral collision rate by an exponentially declining function of altitude as
287 is common in this field. For the electron density, we use an exponentially increasing function of
288 altitude, also common in the field [see, e.g., Eq. 3.23, Section 3.2.3, in Volland, 1995]. See Table
289 1 for details.

290

291 Figure 1 summarizes the prediction of our plane-wave reflection model. The vertical axis is the
292 amplitude reflection coefficient, R , from the D-layer for a typical long-range-propagation angle
293 of incidence, in this case chosen as 85 deg. The reflection coefficient shown has been averaged
294 over all frequencies from 5 to 20 kHz. As shown in JHB1, R varies continuously with solar
295 zenith angle, but we show the pure-day and pure-night extreme cases only. On the left of Figure
296 1 is shown (a) the day-profile D-layer result, while on the right is shown (b) the night-profile D-
297 layer result (refer to Table 1 for profile parameters). The abscissa is the wave magnetic
298 propagation azimuth. A separate curve is shown for each abs(dip angle), from 5 deg (blue) to 85
299 deg (red), in steps of 5 deg. The curves for dip = 30 deg and 45 deg are labeled in the night
300 profile. For both (a) and (b), the curve for dip = 45 deg is dashed. The horizontal black line
301 marks the nadir of the night-profile reflectivity level for dip = 45 deg.

302

303 How do we employ the single-reflection reflectivity from a plane-wave model, in the context of
304 long-range ("multi-hop") propagation of quasi-cylindrical waves in a spherical-shell waveguide?

305 The article on the first half of this project, JHB1, shows how this is done heuristically but with
 306 satisfactory agreement with observations: First, we correct the wave amplitude for the varying
 307 cross-sectional area of a ray-bundle on the spherical Earth (see Eq. 7 in JHB1). Second, we rely
 308 in JHB1 on a free parameter "r", which is the effective number of reflections per reference
 309 distance $\rho_0 = 1000$ km (= 1 Mm). In JHB1 we demonstrated how comparison with observed
 310 received electric-field amplitude resulted in a fit for r in the range $3 > r > 2$.

311
 312 Those two heuristics (correcting for the ray-bundle area, and invoking an effective reflection-
 313 per-pathlength) were used in JHB1 to crudely approximate long-range waveguide transmission
 314 in terms of the single-hop, plane-wave reflectivity model. We define a "logarithmic reference
 315 transmission", *assuming perfect ground conductivity*, along the Great Circle Path segment $L_{i,m}$
 316 from VLF emission point "m" to sensor point "i" :

$$317 \ln(\text{ref. transmission}) = \frac{1}{\rho_0} \int_0^{L_{i,m}} \ln(R[Z_{i,m}(t_0), \alpha_{i,m}, I_{i,m}]) ds_{i,m} + C(L_{i,m}) \quad \text{Eq. (1)}$$

318 where

319
 320 $L_{i,m}$ = arcdistance along Great Circle Path from lightning location m to station i

321
 322 $Z_{i,m}(t)$ = time-dependent, location-dependent solar zenith angle along path i,m

323
 324 $\alpha_{i,m}$ = location-dependent magnetic propagation azimuth along path i,m

325
 326 $I_{i,m}$ = location-dependent magnetic dip angle along path i,m

327
 328 $R(Z_{i,m}(t), \alpha_{i,m}, I_{i,m})$ local instantaneous plane-wave reflectivity

329
 330 $ds_{i,m}$ = differential path element along Great Circle Path i,m

331
 332 $\rho_0 = 1000$ km

333

334 The term $C(L_{i,m})$ in Eq. (1) is the geometrical correction due to the variation of ray-bundle cross-
 335 sectional area. We tabulate the correction, relative to its value at the reference distance 1000 km:

$$336 C(L_{i,m}) = \ln \left\{ \sqrt{\frac{\sin(\rho_0/R_E)}{\sin(L_{i,m}/R_E)}} \right\} \quad \text{Eq. (2)}$$

337 where R_E is the Earth's radius.

338 The logarithmic reference transmission (Eq. 1) must be multiplied by the fitted parameter r to
 339 give an estimate of the actual logarithmic path transmission *assuming zero ground losses* (see
 340 Eq. 9b in JHB1). This r parameter was fitted to lie in the range of 2 to 3. Physically, it is the

337 number of hops per 1000 km reference distance, subject to our model's assumption of 85-deg
338 angle-of-incidence.

339
340 Ignoring ground losses would be unacceptable if we were trying to calculate absolute
341 transmission in the waveguide. However, our application involves examining the difference
342 between day and night conditions on the propagation anisotropy. The ground conductivity effects
343 are unchanged (on a given path) between day and night. Thus modeling only D-layer losses is a
344 satisfactory (though not perfect) approach for our study of day-versus-night differences.

345
346 A further convenient simplification introduced in JHB1 is that we actually solve for the log
347 reflectivity $\ln(R)$ only for the two extreme cases of pure day and pure night. Any intermediate
348 case is approximated by a linear combination of pure-day and pure-night, using a smooth
349 function of solar zenith angle (see Eqs. 10-11 in JHB1). *This is done locally, at each point along*
350 *the path integral in Eq. (1), and for local solar zenith angle obtaining at the instant of the*
351 *lightning stroke.* There is a crucial difference between, on the one hand, making the linear
352 combination locally (which we do), versus, on the other hand, evaluating the path integral along
353 the entire path both for an artifactual day and an artifactual night case, then taking a linear
354 combination of those two results based on the proportion of the path that is daylight. The approach
355 latter would be clearly incorrect.

356 357 **3b. Disfavoring of nighttime (relative to daytime) magnetic-westward propagation**

358 Note that for $\text{abs}(\text{dip angle}) < 45$ deg, the night-profile reflectivity (Figure 1b) for propagation
359 toward magnetic west (270 deg) is *less than the day-profile reflectivity (Figure 1a)*. This
360 favoring of daytime over nighttime transmission for $\text{abs}(\text{dip angle}) < 45$ deg actually applies over
361 a broad azimuth sector centered on magnetic west. Thus, for essentially half of all possible dip
362 angles, and for essentially half of all possible propagation magnetic azimuths, the *nighttime*
363 *reflection is predicted by our model [Jacobson et al., 2010; Jacobson et al., 2009] to be*
364 *disfavored relative to the daytime reflection, and for small dip angle deeply disfavored.* This
365 surprising and counter-intuitive feature is not remarked elsewhere in the VLF literature, and thus
366 the burden is on us to provide observational support for this counter-intuitive claim. Intuition
367 would suggest that nighttime propagation should be *less* lossy than daytime, because the
368 nighttime reference height (85 km in our model) has only 17% as much electron-neutral collision
369 rate as does the daytime reference height (73 km in our model).

370
371 The remainder of this article relies on the first part of the study (JHB1) for a detailed
372 development of the model theory. Readers should consult JHB1, which was published as Open
373 Access and hence is without cost to the reader.

374 375 **3c. Summary of observational results from part 1 of the present study**

376 We presented in JHB1 a method to study the behavior of the inter-station ratio of VLF stroke
377 amplitudes, for strokes that are simultaneously recorded at multiple WWLLN stations. This
378 approach combined numerous recurrent strokes from long-duration lightning clusters to build a
379 time-series of the ratio for a major portion of the UT day. The time variations of the sliding-
380 averaged ratio are dominated by transient excursions coinciding temporally with those periods
381 when the solar terminator is present along one or both of the paths. See, e.g., Figure 2 in JHB1.
382 This strongly motivates a model incorporating significant control by the solar zenith angle.

383
384 Our plane-wave model predicts that magnetic-westward propagation has less waveguide
385 transmission than does magnetic-eastward propagation. *Crucially, the anisotropy is extremely*
386 *magnified for a night ionosphere.* This anisotropy is modulated by magnetic dip angle: The
387 anisotropy is strongest at low dip angle, and weakest at large dip angle.
388

389 To account for solar-zenith-angle control on the waveguide transmission, our model takes a
390 weighted combination of pure-day and pure-night solutions, *determined locally for every path*
391 *element along the Great Circle Path from the lightning to the WWLLN station, and for the exact*
392 *Universal Time of the stroke.*
393

394 The model solution based on the plane-wave-reflection theory successfully accounted for the
395 gross features of the solar-terminator transients; see, e.g, Figures 7-10 in JHB1.
396

397 Our model predicts, counter-intuitively, that the magnetic-westward attenuation at low magnetic
398 latitude will be much deeper during night than during day conditions. Unfortunately, this
399 suppression of magnetic-westward propagation also largely eliminates the availability of
400 sufficiently numerous recurrent recordings of those signals at our low-latitude stations. Thus the
401 amplitude-ratio method pursued in JHB1 was inherently unable to check on the model's most
402 intriguing and counter-intuitive prediction.
403

404 Thus our method to follow, rather than using lightning detections that exist, is designed to
405 demonstrate the pattern of where and when detections do *not* exist.
406

407 **4. WWLLN evidence on day/night differences in anisotropic VLF propagation**

408

409 **4a. WWLLN database**

410 The overall epoch for this study is 1 December 2009 through 31 May 2021, Universal Time
411 (UT). Within that overall epoch, numerous WWLLN recording stations began operation,
412 occasionally interrupted operation, and (in a few cases) ceased operation. For much of the overall
413 epoch, at any time WWLLN had > 50 active stations worldwide. At present (2021) the census is
414 > 60 active stations.
415

416 Our methodology in the following is to develop statistics on the *patterns of detection and non-*
417 *detection by selected stations.* We use the entire WWLLN network product to define the overall
418 population of WWLLN-located lightning strokes. This population is defined in a separate day
419 file for each UT day. We then focus on ten selected stations located at magnetic low and mid
420 latitudes. We develop statistical maps of the detection/non-detection of the overall WWLLN
421 stroke population, by each of these ten selected stations. Table 2 lists pertinent metadata about
422 the ten selected stations. Three of the stations (Atuona, Tahiti, and Honolulu) are in the Pacific
423 ocean and have dominantly over-seawater paths from abundant lightning in both their Eastern
424 and Western sectors. Another station (Costa Rica) is on a relatively narrow land bridge between
425 major oceans. Two stations (Peru and Dakar) are on the western periphery of lightning-rich
426 continents.
427

428 For the statistics on each of the ten selected stations, we define a latitude band within which to
429 include WWLLN strokes. This band is -40 to +40 deg N for nine of the stations, but for
430 Honolulu the band is displaced to -30 to +50 deg N, in order to include the strokes in the
431 northern continental United States. The population of WWLLN strokes within the latitude band
432 is used to detect detection/non-detection by the respective selected station.
433

434 The population of WWLLN strokes within the latitude band and available for detection by the
435 respective selected station varies from a maximum of $> 2 \times 10^9$ strokes (for both Honolulu and
436 Tel Aviv) down to 3.2×10^8 strokes (for Belem). This disparity is driven mainly by the difference
437 between the number of operating days for Honolulu (3873) or for Tel Aviv (3987), versus for
438 Belem (566) within the overall epoch.
439

440 **4b. Qualitative demonstration of geomagnetic and zenith-angle control over detection**

441 Before embarking on a systematic quantitative analysis, we show a qualitatively clear example of
442 the control over detection exerted by solar zenith angle and by geomagnetic parameters. Figure 2
443 shows the case of Atuona station, near the mid-Pacific. This example conveniently illustrates the
444 situation for low dip angle and nearly-zonal magnetic propagation azimuth everywhere along the
445 paths eastward and westward to regions of abundant lightning. In Figure 2, the station is a black
446 rectangle symbol. In Figure 2(a), to the East of Atuona is shown a red rectangular box in
447 northwestern South America. We select all WWLLN strokes within that box. For each stroke
448 within that box, we calculate the solar zenith angle (at D-layer height) for all points along the
449 path to Atuona from the stroke, and characterize each stroke by the proportion of the path that is
450 in daylight. Figure 2(b) shows the daylit-fraction distribution of all strokes in the red box of
451 Figure 2(a). The distribution is flat except for roughly equal peaks both at pure-dark (daylit
452 fraction = 0) and at pure-daylit (daylit fraction = 1). We now ask, what is the Atuona detection
453 efficiency (DE) for these strokes, versus the daylit fraction parameter? This is shown in Figure
454 2(c). The DE peaks toward maximum daylight, and is suppressed (by an order of magnitude) for
455 daylit fraction < 0.6 .
456

457 Now let us define a "control" case, which is shown in the right column of Figure 2. Figure 2(d)
458 shows in red a "West box" over the Australasia sector. It is slightly further from Atuona than the
459 East Box, but is roughly comparable in dip angle along the paths to Atuona. Figure 2(e) shows
460 the daylit-fraction distribution for all strokes in the West box. Figure 2(f) shows the DE for
461 Atuona detection of those strokes, as a function of daylit fraction. Now the DE for eastward
462 propagation is relatively indifferent to daylit fraction, and the median DE for the west box is two
463 orders-of-magnitude higher than the median DE for the East box (Figure 2c), and one order-of-
464 magnitude greater than the maximum DE for the East box (Figure 2c). We note that this is a case
465 where the paths to Atuona from either the West or the East box are everywhere quasi-zonal in
466 magnetic azimuth, and are everywhere at very small dip angle (-20 deg to +20 deg). We chose
467 this because of its convenience for a qualitative exercise like Figure 2.
468

469 This example qualitatively demonstrates, within the context of low dip angle, (a) the dramatic
470 difference between propagation at eastward magnetic azimuth versus westward magnetic
471 azimuth, and (b) the extreme favoring of daylit propagation over night propagation for westward
472 magnetic azimuth. This latter feature has not previously been remarked in the VLF literature.
473

474 **4c. Geomagnetic context for the ten selected stations**

475 We now show the geomagnetic context of each of the ten selected stations and of the propagation
476 paths connecting them to lightning strokes in their respective latitude band described in Table 2.
477 The geomagnetic model is the International Reference Geomagnetic Field, or IGRF [*V-MOD*,
478 2010]. Figure 3 contains a separate panel for each of the ten stations. Color indicates the
479 geomagnetic dip angle's absolute value, in deg. Black is dip = 0 deg. For nine of the panels, red
480 is 74 deg, while for one (Figure 3i, Honolulu) the band is offset and the maximum dip angle is 76
481 deg. In addition to color-coding, discrete curves of $|\text{dip}| = 30, 45$ deg are overlaid on the map.
482 The station is marked with a rectangle symbol, either white or black, to contrast with its
483 immediate background color. The color shading covers the latitude band in which strokes are
484 considered for detection/non-detection by the respective station.

485
486 Because of the extremely low transmission of VLF over Antarctic (or, to a lesser extent, Arctic)
487 ice, we wish to exclude strokes whose Great Circle paths to the selected station reach further
488 poleward than geographic latitude +/- 55 deg. This excludes strokes roughly within a cone
489 centered on the respective station's antipode, which we blank-out with white. Thus, for example,
490 in Figure 3(a) the antipode of Atuona is situated near the southern Red Sea. Each station has its
491 own antipode, and cone centered there, in which we do not gather statistics regarding stroke
492 detection by that station.

493
494 Recall that the model results (Figure 1) predict a nighttime increase of attenuation for
495 propagation toward magnetic West, relative to daytime, for $|\text{dip angle}| < 45$ deg. This nighttime
496 increase in attenuation toward magnetic West becomes especially severe for $|\text{dip angle}| < 30$ deg.
497 Figure 3 shows visually that this band of enhanced nighttime westward attenuation occupies
498 most of the important lightning prone areas [*Christian et al.*, 2003], excepting only the
499 continental United States. That is, the nighttime disfavoring of magnetic-westward VLF
500 propagation is not going to be a mere academic curiosity confined to a small region, but rather
501 applies to most regions of relevance to global VLF lightning location.

502 503 **4d. Spatial patterns of observed and predicted detectability**

504 **4d.1 Approach**

505 We now start a formal comparison of the observed and predicted detection patterns of each of the
506 ten selected stations. Separately for each station, we define two cohorts of strokes within the
507 accepted latitude band. The first cohort contains the strokes whose Great Circle Paths to the
508 station are $> 80\%$ sunlit at the instant of the stroke, at D-layer height. This first cohort represents
509 mostly-daytime propagation. The second cohort contains the strokes whose Great Circle Paths to
510 the station are $< 20\%$ sunlit, representing mostly-nighttime propagation.

511
512 In addition to those statistics based on observation, we calculate the logarithmic reference
513 transmission (Eq. 1 above) for each Great Circle Path under two artificial conditions: that the
514 entire path be either in daylight or in darkness. These yield "day" and "night" logarithmic
515 reference transmissions.

516
517 Finally, we calculate the instantaneous logarithmic reference transmission, *using the actual*
518 *instantaneous solar zenith angle at each point along each path*, for all strokes. The distribution
519 of logarithmic reference transmission shows the strokes that are *available* for the selected station

520 to detect. The sub-distribution of logarithmic reference transmission *only for the strokes that are*
521 *detected by the selected station* shows the relationship between detectability (by the selected
522 station) and logarithmic reference transmission (relative to the selected station). We would
523 expect that if the model has some correlation to observational reality, then the strokes detected
524 by the selected station would be bunched at the high-transmission end of the distribution, and
525 would be sparse or absent in the low-transmission end of the distribution. On the other hand, if
526 the model were basically worthless, then there would be no strong correlation between observed
527 detectability and model-predicted logarithmic reference transmission.

528
529 The reader should keep in mind that stations do not all have the same effectiveness in detecting
530 lightning [Hutchins, 2014]. We will call this "sensitivity", but this does not mean something so
531 simple as system gain. Rather, the two most important factors are, first, the level of background
532 VLF noise affecting the selected station, and, second, the abundance of nearby lightning
533 [Hutchins, 2014]. The effect of abundant nearby lightning is to reduce the ability of the station to
534 participate in network detections of distant lightning strokes. This is because each WLLN
535 station has a software-adjusted trigger threshold for capturing a pulse to become a candidate for
536 participation in a network location of strokes. The threshold is sluggishly (~2 minutes of inertia)
537 adjusted, so as to continuously keep the rate of station triggers not greater than 3 per second.
538 Abundant nearby lightning interacts with this feedback to increase the trigger level and thus
539 reduce the ability of that station to trigger on distant lightning.

540 541 **4.d2 Ten case studies of patterns of detection/non-detection**

542 543 **Atuona case**

544 Figure 4(a) maps the density of the first cohort of strokes, having mostly-sunlit paths to Atuona.
545 The color scale is *relative to the maximum-density pixel in this plot*, with blue meaning
546 0.01Xmaximum, and red meaning maximum. The resolution is 1-deg X 1-deg. The white areas
547 are < 0.01Xmaximum. The stroke density is displayed only within the -40 to +40 deg N band.
548 The curves of |dip angle| = 30, 45 deg are shown in heavy black, while the geomagnetic equator
549 is shown as a thinner black curve. Neither the |dip angle| curves, nor the stroke density, are
550 shown within the antipodal cone. Also, the -45 deg dip-angle curve is not shown where
551 (southmost South America) it is outside the latitude band.

552
553 Figure 4(b) is like Figure 4(a), *except that the density is only for the subset of the day-cohort*
554 *strokes that are detected by Atuona*. Thus comparison of Figure 4(a, b) gives a visual map of the
555 pattern of day-cohort detection/non-detection by Atuona. Note that the eastern two-thirds of
556 South America's day-cohort lightning is not detected by Atuona, whilst the lightning in SE Asia
557 and Indonesia, though no closer, is largely detected.

558
559 Reminder: The color range in the second panel, Figure 4(b), is determined *only* by the densities
560 in Figure 4(b), and is *unrelated* to the color range in the first panel, Figure 4(a). Thus for
561 example, the threshold for blue (0.01Xmaximum) is different (and smaller) in Figure 4(b) than in
562 Figure 4(a). This allows blue cells to appear in the second panel, in principle, at a few locations
563 that are white (sub-blue) in the first panel.

564

565 Figure 4(c) maps the value of the day logarithmic reference transmission, for all grid points
566 within the selected latitude band, regardless of the incidence of lightning there. The only
567 exception is that the transmission is whited-out in the antipodal cone. The displayed value is
568 lumped into just four ranges of logarithmic reference transmission: > -2 (red), -2 to -3 (yellow), -3
569 to -4 (green), and < -4 (blue).

570

571 Figures (4d-e) are exactly like Figures 4(a-b) except for the second cohort of strokes, having
572 mostly dark paths to Atuona. Figure 4(f) is like Figure 4(c), except for the *night* logarithmic
573 reference transmission. In night conditions, the asymmetry becomes more dramatic. Atuona
574 detections in South America become insignificant. Comparing Figures 4(c,f), we see that the
575 model prediction is consistent with observations.

576

577 Figure 4(g) shows histograms of the actual *instantaneous* logarithmic reference transmission,
578 taking account of the *instantaneous solar zenith angle at each point along the path*. This is not
579 the contrived "day" or "night" prediction of Figures 4 (c,f). The black curve in Figure 4(g) is for
580 all 9.21×10^8 strokes within the latitude band, while the red curve is for only the 1.09×10^8
581 strokes in that band detected by Atuona. By comparing the two curves, it is apparent that
582 Atuona's detection rate falls off rapidly for logarithmic reference transmission < -2 , and is
583 completely insignificant for < -4 . These are empirical facts based on the distribution of lightning
584 amplitudes, the proximity of the lightning to Atuona, the performance of the network, and the
585 performance of this particular station. The empirical evidence of Figure 4(g) allows us to
586 interpret the model predictions for contrived pure-day (Figure 4c) and contrived pure-night
587 (Figure 4f). The red-shaded regions correspond to logarithmic reference transmission > -2 . We
588 can thus interpret the red regions in Figures 4(c,f) as having unimpeded detectability (at least as
589 far as D-layer effects are concerned.) The yellow-shaded regions are predicted to have relatively
590 lower detection success, though not zero. Green is even lower, and there are predicted to be
591 essentially no detections in the blue-shaded regions, where logarithmic reference transmission is
592 < -4 . With that as a guide, we can now appreciate that the behavior of Figure 4(b), relative to
593 Figure 4(a), is roughly consistent with the contrived day model (Figure 4c) and the empirical
594 distribution (Figure 4g). Similarly, the behavior of Figure 4(e), relative to Figure 4(d), is roughly
595 consistent with the contrived night model (Figure 4f) and the empirical distribution (Figure 4g).
596 Notably, Atuona's complete non-detection of any lightning in South America for mostly-dark
597 paths (Figure 4e) is consistent with the all-blue shading of South America (Figure 4f) in the night
598 model. Likewise, Atuona's strong detection in the Australasia sector for mostly-dark paths
599 (Figure 4e) is consistent with that region's being shaded red (Figure 4f) in the night model.

600

601 The map-based displays (Figures 4a-f) are useful for illustrating the geographic patterns of
602 detection/non-detection by Atuona for two extreme cases, as well as comparing those patterns
603 with the respective model predictions. However, these map-based displays are extremely
604 complicated to follow, and are patchy in their coverage due to the uneven geographical and
605 temporal occurrence of lightning [Christian et al., 2003].

606

607 Ultimately, the entire quantitative outcome of our data for Atuona can be distilled into the far
608 simpler and clearer Figure 4(g), which uses *all* the available strokes in the latitude band, without
609 parsing for contrived special cases (mostly-day, mostly-dark). The parent distribution (black
610 curve) shows that $> 50\%$ of the network-detected strokes have logarithmic reference

611 transmission (to Atuona) < -3 , whilst by contrast, for the subset detected by Atuona (red curve)
612 there are very few detected strokes in that range. Thus the predictive model is consistent with the
613 pattern of Atuona's detection/non-detection. (We take as axiomatic that large signals tend to be
614 easier to detect than are small signals.)

615

616 **Tahiti case**

617 Tahiti is close to Atuona though at somewhat larger $|\text{dip angle}| \sim 30$ deg. Figure 5 is like Figure
618 4, but for the Tahiti case. Because Tahiti has operated during almost the entirety of the study
619 epoch, it has more strokes both in the parent distribution (1.94×10^9) and the Tahiti-detected
620 distribution (1.93×10^8) compared to Atuona. The Tahiti detections are almost entirely confined
621 to logarithmic reference transmission (to Tahiti) > -2.5 (Figure 5g), consistent with being a less
622 sensitive station than Atuona. Tahiti almost totally fails to detect lightning in the Americas in
623 night conditions (Figure 5e), while Tahiti is highly successful with the Australasia sector.

624

625 Again, as commented earlier in the case of Atuona, all the quantitative evidence is condensed
626 into Figure 5(g); the geographical map presentations are qualitative by comparison. And again,
627 the sharp cut-off of the red curve in Figure 5(g) shows that the model has predictive value for
628 Tahiti detection/non-detection.

629

630 **Peru case**

631 Figure 6 shows the Peru case. This is the first of our two cases on the west margins of lightning-
632 rich continents. Like Tahiti, Peru can detect almost only for predicted logarithmic reference
633 transmission (to Peru) > -2.5 (Figure 6g). In the daytime case (Figures 6a-c), Peru can detect well
634 throughout South America. In the nighttime case (Figures 6d-e), Peru cannot detect strokes in the
635 eastern half of its own continent, even as it detects in far more distant Micronesia. This is well
636 predicted by Figures 6(c,f). All the quantitative outcomes of the data for Peru are summarized in
637 Figure 6(g), and it indicates the model is consistent with the Peru station's detection/non-
638 detection. If the model were fundamentally inconsistent with the observations, then the red curve
639 in Figure 6(g) would not be selective for the high-transmission end of the abscissa.

640

641 **Costa Rica case**

642 Figure 7 shows the Costa Rica case. Costa Rica can detect mostly for predicted logarithmic
643 reference transmission (to Costa Rica) > -2.5 (Figure 7g). During night conditions (Figures 7d-e),
644 Costa Rica loses detection for strokes in much of eastern South America. During those same
645 night conditions, Peru gains detections in the far more distant Australasia and Micronesia sector,
646 where there are few daytime detections (Figures 7a-b). All the quantitative outcomes of the data
647 for Costa Rica are summarized in Figure 7(g), and it indicates the model is consistent with the
648 Peru station's detection/non-detection.

649

650

651 **Belem case**

652 Figure 8 shows the Belem case. One of our least sensitive stations, Belem is essentially unable to
653 detect for strokes whose predicted logarithmic reference transmission (to Belem) < -2.0 (Figure
654 8g). Some of western Africa lightning is detected by day, but nothing by night. This is consistent
655 with the day and night model predictions (Figures 8c,f). All the quantitative outcomes of the data

656 for Belem are summarized in Figure 8(g)), and it indicates the model is consistent with the
657 Belem station's detection/non-detection.

658

659 **Dakar case**

660 Figure 9 shows the Dakar case. Like Peru, Dakar lies on the western edge of a lightning-prone
661 continent. Figure 9(g) shows that Dakar cannot detect lightning whose predicted logarithmic
662 reference transmission (to Dakar) < -2.0 . During daytime Dakar can detect strokes in all but the
663 easternmost part of Africa (Figures 9a-b), but during the night, Dakar loses all of Africa
664 coverage save for the western bulge proximal to the station itself (Figures 9d-e). All of these
665 effects are consistent with Figures 9(c,f,g). The model predictions are grossly consistent with the
666 Dakar pattern of detection/non-detection.

667

668 **Pune case**

669 Figure 10 shows the Pune case. Pune is between the Australasia's and Africa's lightning-prone
670 regions. As seen in Figure 10(g), Pune's detections are almost all for strokes whose predicted
671 logarithmic reference transmission (to Pune) > -2.3 . During nighttime (Figure 10e) but not
672 during daytime (Figure 10b), Pune can detect significant lightning in South America. Similarly,
673 during nighttime (Figure 10e) Pune cannot detect lightning further east than Thailand, while in
674 daytime (Figure 10b), Pune's detection extends further eastward over Borneo. These are
675 predicted by the model in Figures 10(c,f,g). The model predictions are consistent with the pattern
676 of Pune detections/non-detections.

677

678 **Singapore case**

679 Figure 11 shows the Singapore case. Similar to Pune, Singapore detections are mostly confined
680 to strokes whose predicted logarithmic reference transmission (to Singapore) > -2.3 (Figure 11g).
681 The geographical patterns for the night cohort of strokes show extreme asymmetry favoring
682 strokes on the West of the station and disfavoring strokes on the East of the station. The pattern
683 of detection/non-detection by Singapore is grossly consistent with the model predictions (Figures
684 11 c,f,g).

685

686 **Honolulu case**

687 We complete this survey with two cases where the selected station is at higher magnetic latitude
688 than so far. Figure 12 shows the Honolulu case. The bulk of Honolulu's detections are for strokes
689 whose predicted logarithmic reference transmission (to Honolulu) > -2.5 (Figure 12g), with a
690 low tail out to -4 , as had been the case with Atuona. For the nighttime cohort of strokes (Figures
691 12d,e), Honolulu detects very few strokes in South America, whilst its more distant detections on
692 the West go all the way across India. The Honolulu patterns of detection/non-detection are
693 grossly consistent with the model predictions (Figures 12c,f,g).

694

695 **Tel Aviv case**

696 Finally, Figure 13 shows the Tel Aviv case, located at dip angle > 45 deg. Virtually all of Tel
697 Aviv's detections are for strokes whose predicted logarithmic reference transmission (to Tel
698 Aviv) are > -2.5 (Figure 13g). Despite its relatively high magnetic latitude, long range detection
699 eastward or westward into the low magnetic latitudes still displays the asymmetry favoring
700 strokes from South America over strokes in Australasia, particularly for the night cohort (Figure

701 13e). The Tel Aviv pattern of detection/non-detection is grossly consistent with the model
702 predictions (Figures 13c,f,g).

703

704 **4e. Closing the observational case that the model is consistent with the data**

705 We have presented observations of the geographical patterns of detection/non-detection for ten
706 selected stations around the globe, at low and low-middle latitudes. The geographical patterns
707 are shown for separately for mostly-day, and then mostly-night transmission paths. The observed
708 patterns of detection/non-detection are consistent with the patterns of predicted logarithmic
709 reference transmission, for the respective day or night cases. More quantitatively, the
710 distributions of actual logarithmic reference transmission to each selected station, both for the
711 parent distribution and for the subset of strokes in whose location the selected station is a
712 participant (i.e. detected by the selected station), show that the paths for *detected* strokes are
713 clustered at the high-transmission end of the parent distribution. Thus the model predicts which
714 cases are more likely to be detected, and which are not.

715

716 As mentioned earlier, this logic rests on an axiom: All other things being equal, a strong pulse is
717 more likely to be detected than is a weak pulse. And we assume, all other things being equal, that
718 paths involving relatively weaker transmission will cause weaker detected pulses than will paths
719 involving relatively stronger transmission.

720

721 We now perform a "sanity check" on this key assumption. Figure 14 shows distributions of the
722 detected, raw ADC amplitudes for pulses detected by the Tel Aviv station. The ADC is 16-bits
723 deep (0 to 65535), but we show the distributions out to only ADC level 5000. The two panels in
724 Figure 14 are for two adjacent tranches of modeled logarithmic reference transmission: (a) > -2 ,
725 and (b) in the range -2 down to -2.5 . The shoulder at about ADC level 100 - 200 corresponds to
726 the local-time servo adjustments of the station's software trigger threshold. The higher-
727 transmission distribution (a) contains 1.8×10^8 detections, while the lower-transmission
728 distribution (b) contains only $\sim 12\%$ as many detections. Moreover, in (a) the high-transmission
729 distribution's tail, relative to the distribution's peak, is much more relatively populated than in
730 (b). Finally, whereas in (a) the peak occurs at ADC level ~ 800 , in (b) it has retracted to ~ 500 .

731

732 Thus Figure 14 supports the picture that the high-transmission population's extended tail (to
733 higher values of detected ADC level) becomes depleted at lower transmission, with those tail
734 members being swept to the left end of the distribution. Most of those then are swept to sub-
735 threshold ADC level, but some remain above the threshold and constitute the peak in (b). Let us
736 see if this picture makes quantitative sense. The change in logarithmic reference transmission
737 between these two tranches is in the range 0.5 to 0.75, depending on where, within a tranche, it is
738 figured. The first part of this study demonstrated that the "r" parameter, which multiplies the
739 logarithmic reference transmission to give the actual physical transmission, was fitted by the data
740 of JHB1 to lie in the range from 2 to 3 Nepers (see Figures 6 and 9, and discussion thereof, in
741 JHB1). Let us choose 2.5 Nepers. Then the change in logarithmic reference transmission
742 between these two tranches in the range 0.5 to 0.75 Nepers corresponds to a change in *physical*
743 logarithmic transmission in the range 1.25 to 1.88 Nepers. In linear amplitudes, the range is a
744 multiplicative factor from ~ 3.5 to ~ 6.5 . This implies that the transition from Figure 14(a) to
745 14(b) can be understood as taking tail members in (a) and moving them leftward (to lower ADC
746 level) in (b) down to ADC levels only $1/3.5$ to $1/6.5$ as big. Fortunately, we see that the tail in (a)

747 contains sufficient population to permit this simple occur. Thus the relative distributions of
748 detected raw ADC levels are consistent with the predicted transmissions of adjacent tranches of
749 the transmission distribution.

750

751 **5. Conclusions**

752

753 This is the second part of a two-part study of broadband VLF propagation from lightning strokes
754 to WWLLN stations. The first part of the study (JHB1) had developed a model for the effects of
755 the ionospheric D-layer on long-range VLF transmission in the Earth-Ionosphere Waveguide.
756 The model makes the counter-intuitive prediction that, for dip angles in the range -30 to +30 deg,
757 propagation toward the west half of magnetic azimuths will be dramatically worse during
758 conditions of darkness (along the propagation path) than during conditions of daylight. This
759 feature had never been remarked before in the literature, although it is in fact also embedded in
760 the standard LWPC code. We surmise that the reason the feature had never been remarked is that
761 the LWPC is an end-to-end treatment that tends to obscure, to the code's user, the details of
762 differential transmission at any one point on the propagation path.

763

764 Our model had been applied in JHB1 to explaining the inter-station ratios of signal amplitudes
765 from the same stroke at different stations. That approach, in common with all virtually all other
766 approaches done by prior workers, was based on the measurement of VLF amplitudes. However,
767 we found that the amplitude-based method was inadequate to the test the model's counter-
768 intuitive prediction regarding the day/night control of westerly propagation. That is because the
769 amplitude-based approaches require detections in order for amplitudes to be determined. "No
770 detections, no amplitudes".

771

772 This second part of the study circumvents that problem by adopting an opposite approach. Rather
773 than use received signal amplitudes as the raw data, we now use the observed statistical patterns
774 of detection/non-detection. We compare those patterns to our model's predictions of the D-layer
775 contributions to path transmission. By focusing on the variations between daylit and dark
776 conditions, we also avoid the confounding effect of ground losses, as the latter are invariant
777 between daylit and dark conditions.

778

779 We highlight the geographical patterns of detection/non-detection from each of ten selected
780 stations arranged around diverse longitudes. For each of these stations, we identify strokes whose
781 paths are either mostly daylit or mostly dark. The patterns of detection/non-detection in these
782 two special cases are then compared with the predictions of our transmission model, for either
783 all-lit paths or all-dark paths respectively. The spatial agreement between observation and model
784 is good. We then use *all* the strokes, not just those whose paths are mostly lit or mostly dark, and
785 calculate the modeled logarithmic reference transmission along each stroke's path to the selected
786 station, taking account of the instantaneous solar zenith angle at each point along the path. We
787 tally the distribution of logarithmic reference transmission, both for the parent population of
788 strokes, and for the subset of strokes that are detected by the selected station. We find
789 consistently, for all of our ten selected stations, that the detected subset's distribution of
790 logarithmic reference transmission is entirely crowded to the high-transmission end. This
791 suggests that the model's predictions of transmission are pertinent.

792

793 Finally, and most importantly, our ten case studies robustly demonstrate that for dip angles in the
794 range -30 to +30 deg, during conditions of darkness there is dramatically worse transmission
795 from magnetic East to West then from magnetic West to East, whereas for daylight conditions, this
796 is much less pronounced. These findings are operationally significant for long-range lightning
797 detection. For example, WWLLN's Pacific stations Atuona, Tahiti, and Honolulu are not able in
798 dark-path conditions to contribute significantly to locating lightning in South America, though
799 they are extremely useful over comparable distances with lightning in Australasia. Similarly,
800 under dark-path conditions, Peru basically misses the eastern half of its own continent, and
801 Dakar sees even less of its own continent. For the same reason, during dark-path conditions,
802 Pune is very good for detecting lightning in Africa but misses almost all lightning at similar
803 distances in Australasia. These effects are not subtle, when viewed geographically in terms of
804 areas of detection and non-detection.

805

806 **Acknowledgements**

807 The authors are using data from the World Wide Lightning Location Network, a collaborative
808 consortium of over seventy worldwide collaborators, managed at the University of Washington.
809 The data would not exist but for the cooperative efforts of all of WWLLN's participants. For sale
810 to researchers who are not WWLLN participants, WWLLN data are available, at a nominal price
811 to cover overhead costs of running the network, and archiving / distributing the data. To find out
812 about such data access, see <http://wwlln.net/>

813

814

815

816

817

818

819

820 **References**

821

822 Barber, N. F., and D. D. Crombie (1959), V. L. F. reflections from the ionosphere in the presence
823 of a transverse magnetic field, *Journal of Atmospheric and Terrestrial Physics*, 16, 37-45.

824

825 Bickel, J. E., J. A. Ferguson, and G. V. Stanley (1970), Experimental observation of magnetic
826 field effects on VLF propagation at night, *Radio Sci.*, 5(1), 19-25.

827

828 Budden, K. G. (1985), *The Propagation of Radio Waves*, 669 pp., Cambridge University Press,
829 Cambridge.

830

831 Chand, A. E., and S. Kumar (2017), VLF modal interference distance and nighttime D region
832 VLF reflection height for west-east and east-west propagation paths to Fiji, *Radio Science*, 52,
833 1004-1015, doi:10.1002/2016RS006221.

834

835 Christian, H. J., et al. (2003), Global frequency and distribution of lightning as observed from
836 space by the Optical Transient Detector, *J. Geophys. Res.*, 108(D1), 4005,
837 doi:10.1029/2002JD002347, doi:10.1029/2002JD002347.

838

839 Crombie, D. D. (1958), Differences between the east-west and west-east propagation of VLF
840 signals over long distances, *Journal of Atmospheric and Terrestrial Physics*, 12(2-3), 110-117.
841

842 Crombie, D. D. (1966), Further Observations of Sunrise and Sunset Fading of Very-Low-
843 Frequency, *Radio Science*, 1, 47-51, doi:10.1002/rds19661147.
844

845 Cummer, S. A. (2000), Modeling electromagnetic propagation in the Earth-ionosphere
846 waveguide, *IEEE Trans. Antennas Propag.*, 48(9), 1420-1429.
847

848 Hutchins, M. L. (2014), Source, propagation, and effects of lightning in the Earth-ionosphere
849 system, PhD thesis, 156 pp, University of Washington.
850

851 Hutchins, M. L., R. H. Holzworth, C. J. Rodger, and J. B. Brundell (2012), Far-field power of
852 lightning strokes as measured by the World Wide Lightning Location Network, *J. Atmos.*
853 *Oceanic Technol.*, 29, doi: 10.1175/JTECH-D-11-00174, 1102-1110, doi:10.1175/JTECH-D-11-
854 00174.
855

856 Hutchins, M. L., A. R. Jacobson, R. H. Holzworth, and J. B. Brundell (2013), Azimuthal
857 dependence of VLF propagation, *J. Geophys. Res.*, 118, 1-5, doi:10.1002/jgra.50533,
858 doi:10.1002/jgra.50533.
859

860 Jacobson, A. R., R. Holzworth, and X.-M. Shao (2010), Full-wave reflection of lightning long-
861 wave radio pulses from the ionospheric D-region: Comparison with midday observations of
862 broadband lightning signals, *J. Geophys. Res. -Space*, 115, A00E27, doi:10.1029/2009JA014540,
863 doi:10.1029/2009JA014540.
864

865 Jacobson, A. R., R. H. Holzworth, and J. B. Brundell (2021), Using the World Wide Lightning
866 Location Network (WWLLN) to Study Very Low Frequency Transmission in the Earth-
867 Ionosphere Waveguide: 1. Comparison with a Full-Wave Model, *Radio Science*, 56,
868 doi:10.1029/2021RS007293.
869

870 Jacobson, A. R., X. Shao, and R. H. Holzworth (2009), Full-wave reflection of lightning long-
871 wave radio pulses from the ionospheric D-region: Numerical model, *J. Geophys. Res.- Space*,
872 114, A03303, doi:10.1029/2008JA013642, doi:10.1029/2008JA013642.
873

874 Jacobson, A. R., X.-M. Shao, and E. Lay (2012), Time-domain waveform, and azimuth variation,
875 of ionospherically reflected VLF/LF radio emissions from lightning, *Radio Sci.*, 47, RS4001,
876 doi:10.1029/2012RS004980.
877

878 Pappert, R. A., and J. A. Ferguson (1986), VLF/LF mode conversion model calculations for air
879 to air transmissions in the Earth-ionosphere waveguide, *Radio Sci.*, 21, 551-558.
880

881 Pappert, R. A., and L. R. Hitney (1988), Empirical modeling of nighttime easterly and westerly
882 VLF propagation in the Earth-ionosphere waveguide, *Radio Sci.*, 23(4), 599-611.
883

884 Piggott, W. R., M. L. V. Pitteway, and E. V. Thrane (1965), The numerical calculation of wave-
885 fields, reflexion coefficients and polarizations for long radio waves in the lower ionosphere. II,
886 *Phil. Trans. Roy. Soc. Lon.*, 257(1079), 243-271.
887
888 Pitteway, M. L. V. (1965), The numerical calculation of wave-fields, reflexion coefficients and
889 polarizations for long radio waves in the lower ionosphere. I, *Phil. Trans. Roy. Soc. Lon.*,
890 257(1079), 219-241.
891
892 Samanes, J. E., J.-P. Raulin, E. L. Macotela, and W. R. G. Day (2015), Estimating the VLF
893 modal interference distance using the South America VLF Network (SAVNET), *Radio Science*,
894 50, 122-129, doi:10.1002/2014RS005582.
895
896 Taylor, W. L. (1960), VLF attenuation for East-West and West-East daytime propagation using
897 atmospheric, *Journal of Geophysical Research*, 65(7), 1933-1938.
898
899 V-MOD, I. W. G. (2010), International Geomagnetic Reference Field: the eleventh generation,
900 *Geophys. J. International*, 183(3), 1216-1230, doi:10.1111/j.1365-246X.2010.04804.x.
901 Volland, H. (Ed.) (1995), *Handbook of atmospheric electrodynamics*, CRC Press, Boca Raton,
902 Florida, USA.
903
904 Wait, J. R., and K. Spies (1960), Influence of Earth curvature and the terrestrial magnetic field
905 on VLF propagation, *Journal of Geophysical Research*, 65(8), 2325-2331.
906
907 Wait, J. R., and K. P. Spies (1964), NBS Technical Note 300: Characteristics of the Earth-
908 ionosphere waveguide for VLF radio waves, edited by U. S. D. o. C. National Bureau of
909 Standards (now National Institute of Standards and Technology, NBS).
910
911 Yabroff, I. W. (1957), Reflection at a Sharply-Bounded Ionosphere, *Proc. Inst. Radio Engrs.*, 45,
912 750-753.
913
914

915 **Figure captions**

916

917 Figure 1: Model amplitude reflectivity (vertical axis) vs propagation magnetic azimuth
918 (horizontal axis). Color marks magnetic dip angle, from 5 deg (blue) to 85 deg (red). Curve for
919 dip angle = 45 deg is dashed. Model assumes angle-of-incidence is 85 deg, and is averaged over
920 the band 5 - 20 kHz. (a) Day case. (b) Night case, with labels on curves for dip angle = 30, 45
921 deg. The horizontal black line on both panels is through the minimum of the curve for dip angle
922 = 45. deg in (b). See Table 1 for parameter values.

923

924 Figure 2: Comparison of Atuona detection efficiency against strokes in two roughly equidistant
925 geographic boxes. (a) Showing the East box, over northwestern South America. (b) For all
926 strokes in East box, showing the distribution of fraction of instantaneous path (to Atuona) that is
927 daylit. This includes all strokes in the East box, not just those detected by Atuona. Horizontal
928 resolution is 0.01. (c) Detection efficiency (DE) of Atuona against strokes in East box, as a
929 function of the instantaneous daylit fraction of the path. (d) Showing the West box. (e) For all
930 strokes in West box, showing the distribution of fraction of instantaneous path (to Atuona) that is
931 daylit. (f) Detection efficiency (DE) of Atuona against strokes in West box, as a function of the
932 instantaneous daylit fraction of the path. Note the order-of-magnitude difference in DE scales
933 between (c) East and (f) West boxes.

934

935 Figure 3: Geomagnetic setting of each of the ten selected stations. Each station is shown as a
936 rectangle, either white or black so as to contrast with the background. The color shading of the
937 background is magnitude of dip angle, from 0 (black) to 74 deg (red). Only (i) has a different
938 color scale: 0 (black) to 76 deg (red). The colors are shown within latitude bands -40 to +40 deg,
939 except -30 to +50 deg for (i) Honolulu. Also, discrete curves are drawn, where dip angle = -30, -
940 45, +30, and +45 deg. The white cone at each station's antipode is excluded from the analyses,
941 because the Great Circle Paths from strokes within those cones extend poleward of +/- 55 deg
942 latitude.

943

944 Figure 4: Patterns of detection/non-detection for Atuona. (a) Spatial density of WWLLN-located
945 strokes within the latitude band for which the Great Circle Path is > 80% sunlit. The maximum
946 for this density is red, while blue is 1% of the maximum. White areas outside of the antipodal
947 cone correspond to stroke density less than 1% of the maximum. The discrete lines are at dip
948 angle = 0, +/- 30, and +/- 45 deg. Neither the stroke density, nor the curves, are shown within the
949 antipodal cone or outside of the latitude band. (b) Spatial density of the subset of strokes in
950 whose location Atuona participates, for which the Great Circle Path is > 80% sunlit. The new
951 maximum is shown as red, and 1% of this new maximum is shown as blue. (c) Day model
952 logarithmic reference transmission (see text) versus position, in four ranges: > -2 (red), from -2
953 to -3 (yellow), from -3 to -4 (green), and < -4 (blue). Model is not shown within the antipodal
954 cone or outside of the latitude band. (d) Similar to (a) but for Great Circle Paths < 20% sunlit. (e)
955 Similar to (b) but for Great Circle Paths < 20% sunlit. (f) Similar to (c) but for night model. (g)
956 Histogram of logarithmic reference transmission. Black curve: all strokes in latitude band
957 excluding antipodal cone. Red curve: only those strokes in whose location Atuona participates.

958

959 Figure 5: Similar to Figure 4, but for Tahiti station.

960

961 Figure 6: Similar to Figure 4, but for Peru station.
962
963 Figure 7: Similar to Figure 4, but for Costa Rica station.
964
965 Figure 8: Similar to Figure 4, but for Belem station.
966
967 Figure 9: Similar to Figure 4, but for Dakar station.
968
969 Figure 10: Similar to Figure 4, but for Pune station.
970
971 Figure 11: Similar to Figure 4, but for Singapore station.
972
973 Figure 12: Similar to Figure 4, but for Honolulu station. Note that latitude band is -30 to +50
974 deg, for this station only.
975
976 Figure 13: Similar to Figure 4, but for Tel Aviv station.
977
978 Figure 14: Distribution of raw amplitude (ADC level) for WWLLN-located strokes detected by
979 Tel Aviv station. (a) For logarithmic reference transmission > -2.0 . (b) For logarithmic reference
980 transmission from -2.0 to -2.5 .
981
982
983
984
985
986
987
988
989

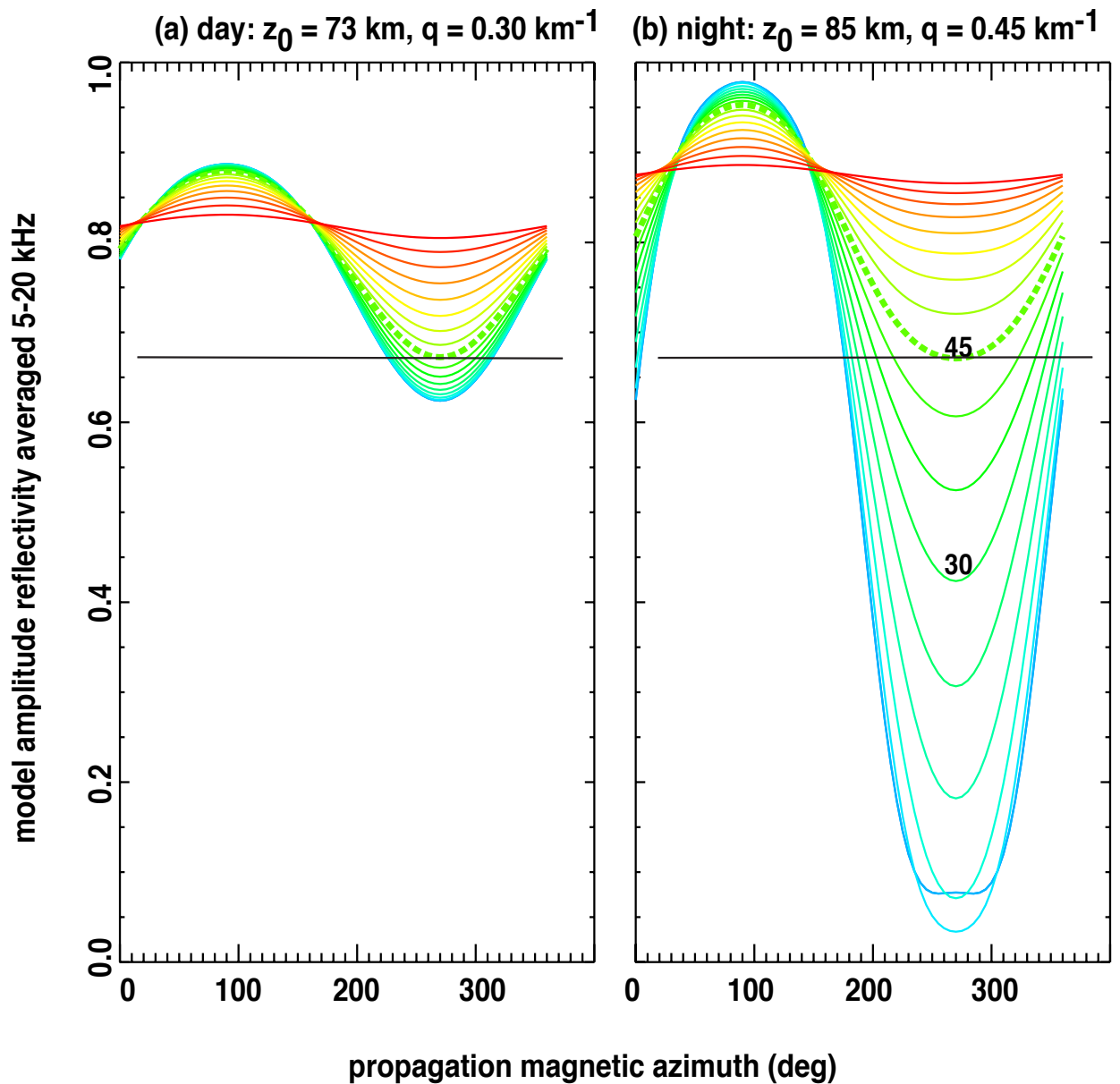


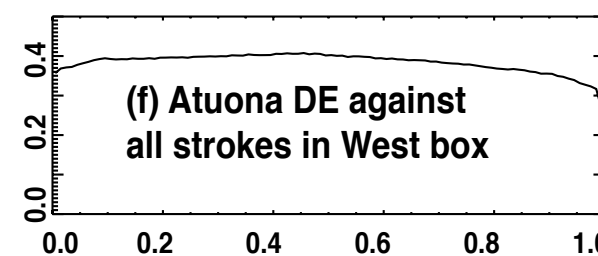
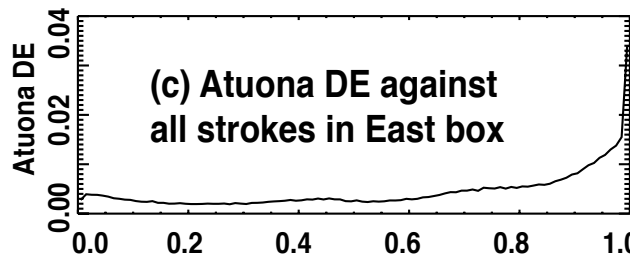
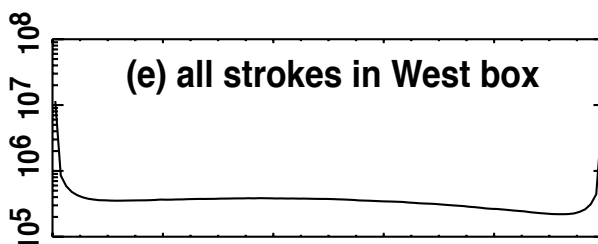
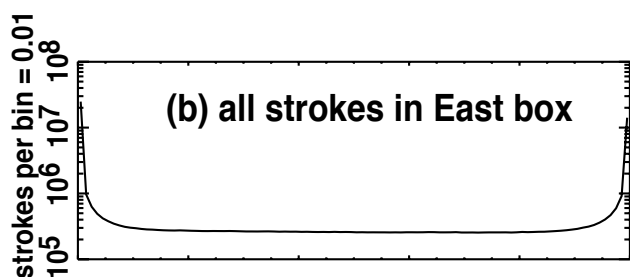
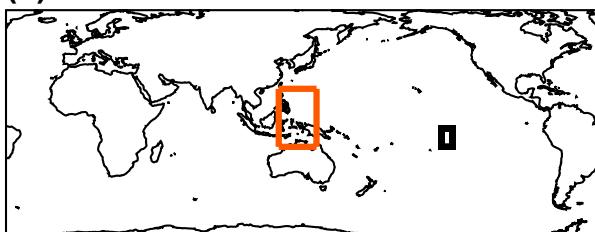
Figure 1: Model amplitude reflectivity (vertical axis) vs propagation magnetic azimuth (horizontal axis). Color marks magnetic dip angle, from 5 deg (blue) to 85 deg (red). Curve for dip angle = 45 deg is dashed. Model assumes angle-of-incidence is 85 deg, and is averaged over the band 5 - 20 kHz. (a) Day case. (b) Night case, with labels on curves for dip angle = 30, 45 deg. The horizontal black line on both panels is through the minimum of the curve for dip angle = 45. deg in (b). See Table 1 for parameter values.

Atuona: 1658 files during 20151030 - 20210531

(a) East box



(d) West box



daylit fraction of Great Circle Path

Figure 2: Comparison of Atuona detection efficiency against strokes in two roughly equidistant geographic boxes. (a) Showing the East box, over northwestern South America. (b) For all strokes in East box, showing the distribution of fraction of instantaneous path (to Atuona) that is daylit. This includes all strokes in the East box, not just those detected by Atuona. Horizontal resolution is 0.01. (c) Detection efficiency (DE) of Atuona against strokes in East box, as a function of the instantaneous daylit fraction of the path. (d) Showing the West box. (e) For all strokes in West box, showing the distribution of fraction of instantaneous path (to Atuona) that is daylit. (f) Detection efficiency (DE) of Atuona against strokes in West box, as a function of the instantaneous daylit fraction of the path. Note the order-of-magnitude difference in DE scales between (c) East and (f) West boxes.

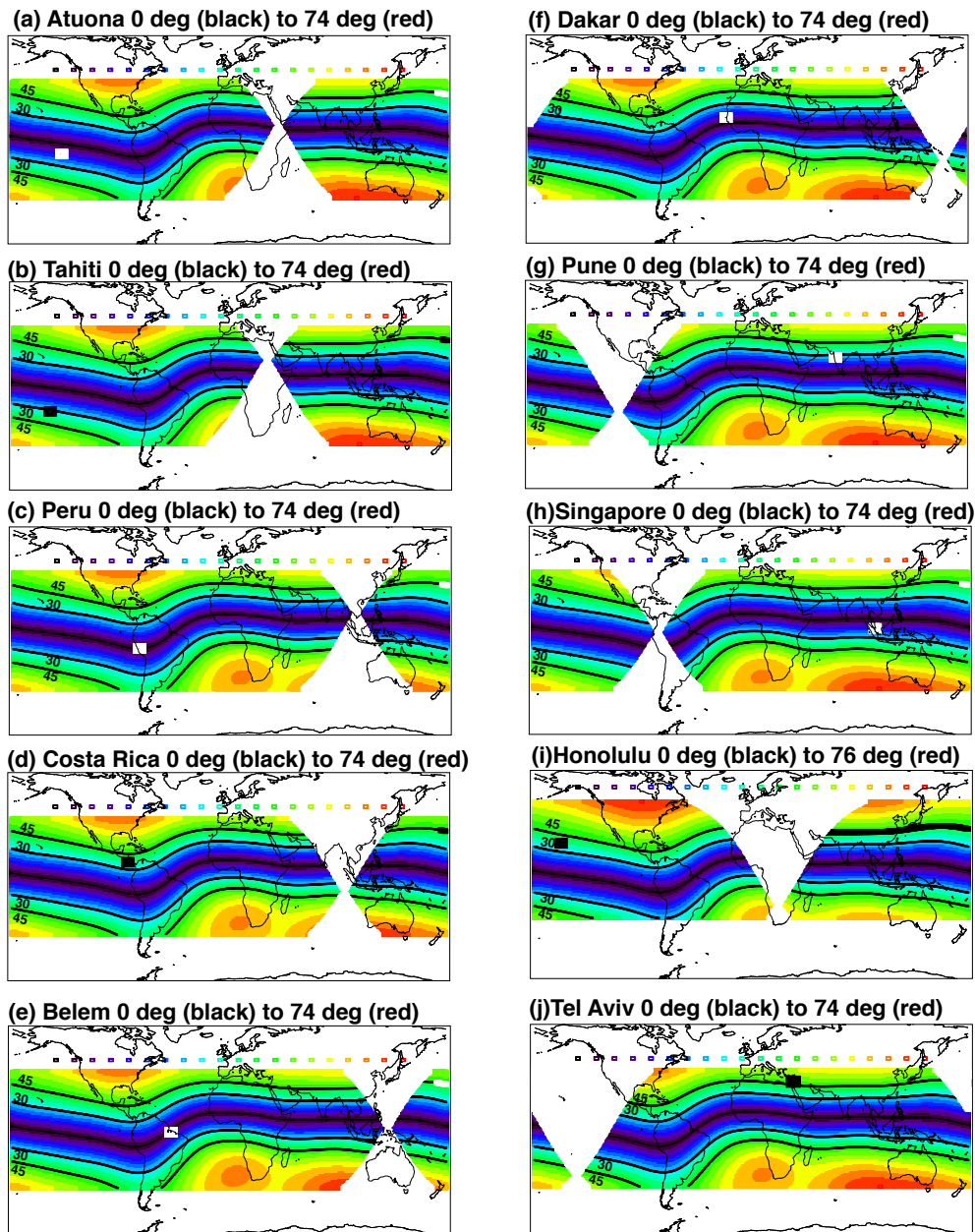


Figure 3: Geomagnetic setting of each of the ten selected stations. Each station is shown as a rectangle, either white or black so as to contrast with the background. The color shading of the background is magnitude of dip angle, from 0 (black) to 74 deg (red). Only (i) has a different color scale: 0 (black) to 76 deg (red). The colors are shown within latitude bands -40 to +40 deg, except -30 to +50 deg for (i) Honolulu. Also, discrete curves are drawn, where dip angle =

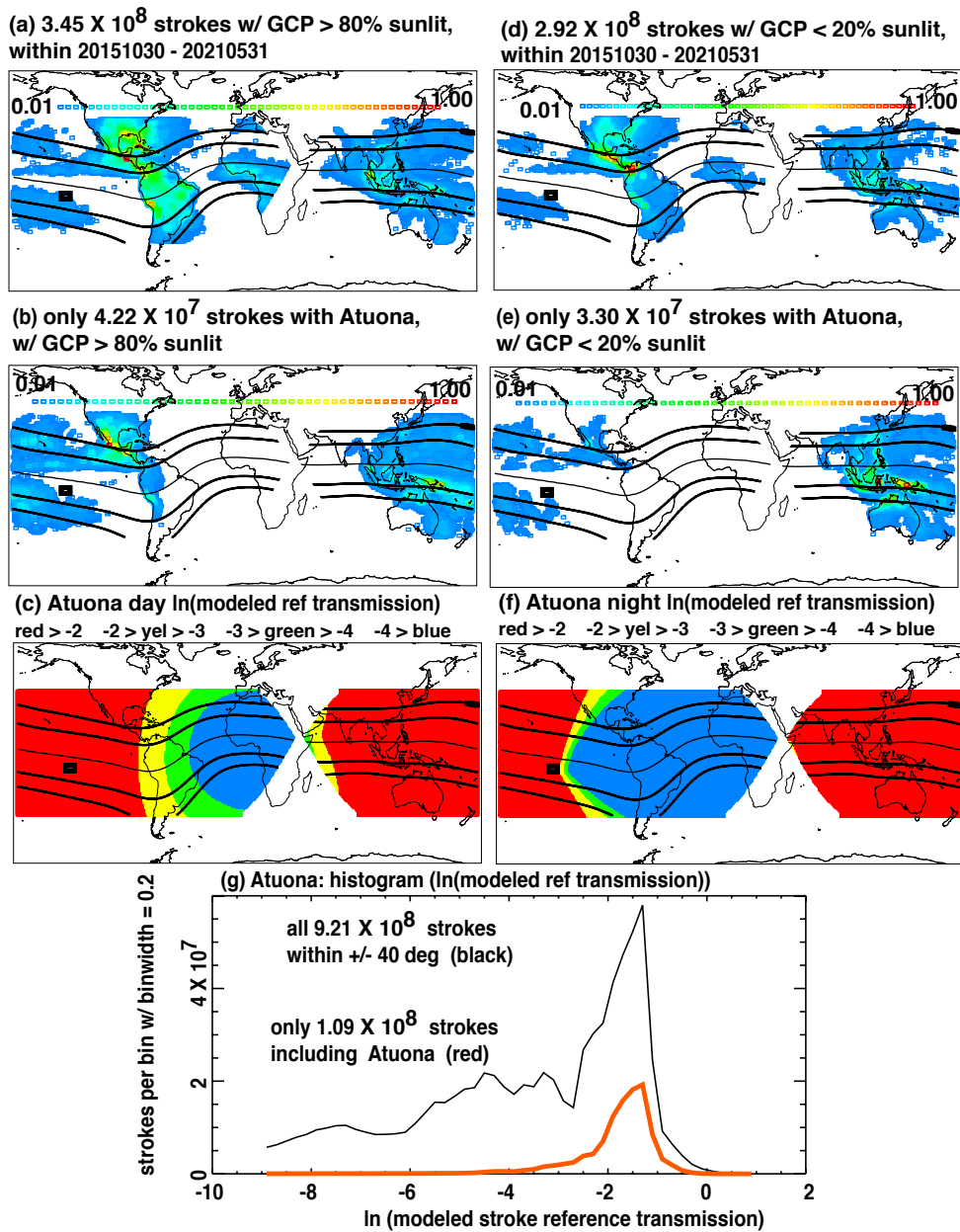


Figure 4: Patterns of detection/non-detection for Atuona. (a) Spatial density of WWLLN-located strokes within the latitude band for which the Great Circle Path is > 80% sunlit. The maximum for this density is red, while blue is 1% of the maximum. White areas outside of the antipodal cone correspond to stroke density less than 1% of the maximum. The discrete lines are at dip angle = 0, ± 30 , and ± 45 deg. Neither the stroke density, nor the curves, are shown within the antipodal cone or outside of the latitude band. (b) Spatial density of the subset of strokes in whose location Atuona participates, for which the Great Circle Path is > 80% sunlit. The new maximum is shown as red, and 1% of this new maximum is shown as blue. (c) Day model logarithmic reference transmission (see text) versus position, in four ranges: > -2 (red), from -2 to -3 (yellow), from -3 to -4 (green), and < -4 (blue). Model is not shown within the antipodal cone or outside of the latitude band. (d) Similar to (a) but for Great Circle Paths < 20% sunlit. (e) Similar to (b) but for Great Circle Paths < 20% sunlit. (f) Similar to (c) but for night model. (g) Histogram of logarithmic reference transmission. Black curve: all strokes in latitude band excluding antipodal cone. Red curve: only those strokes in whose location Atuona participates.

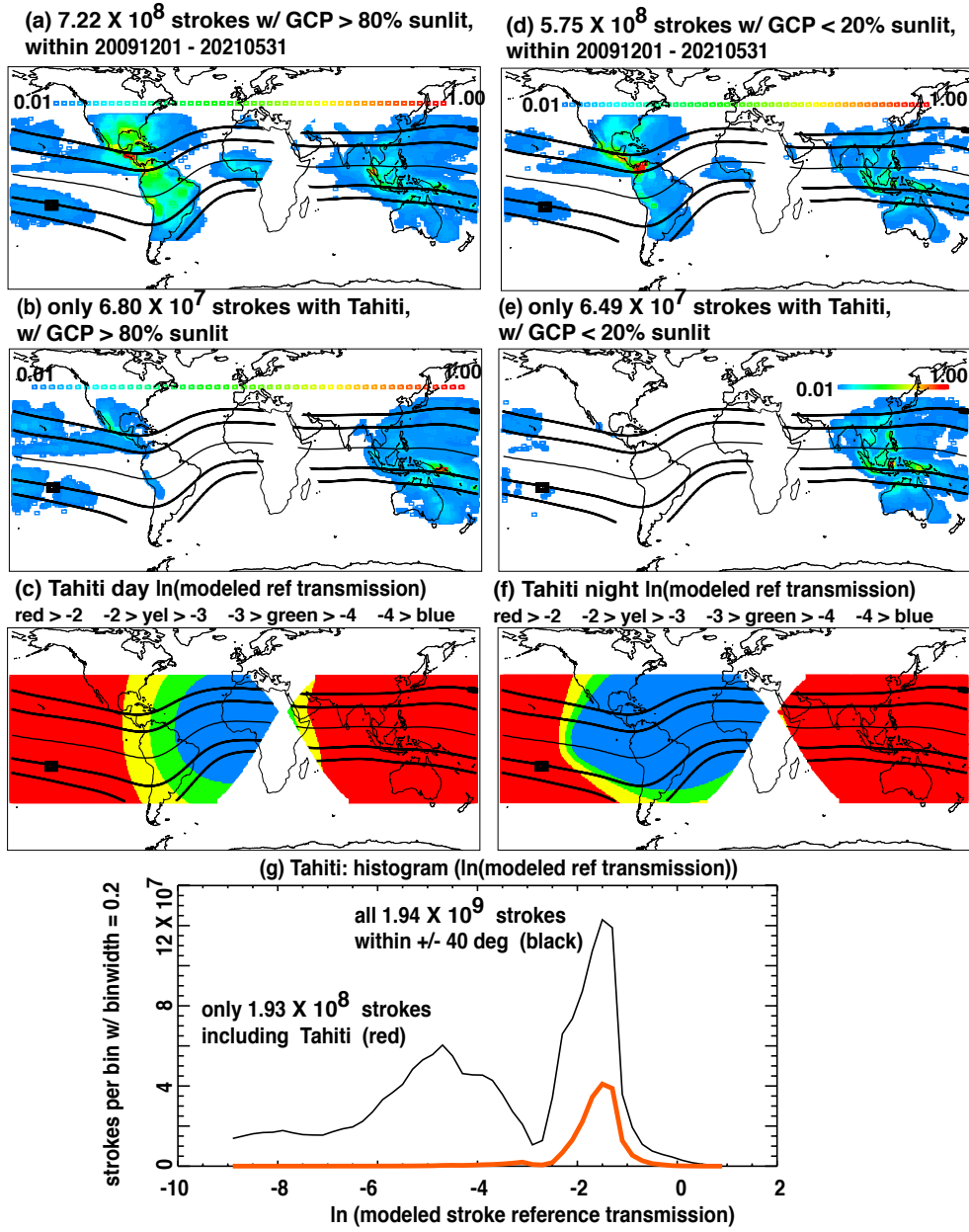


Figure 5: Similar to Figure 4, but for Tahiti station.

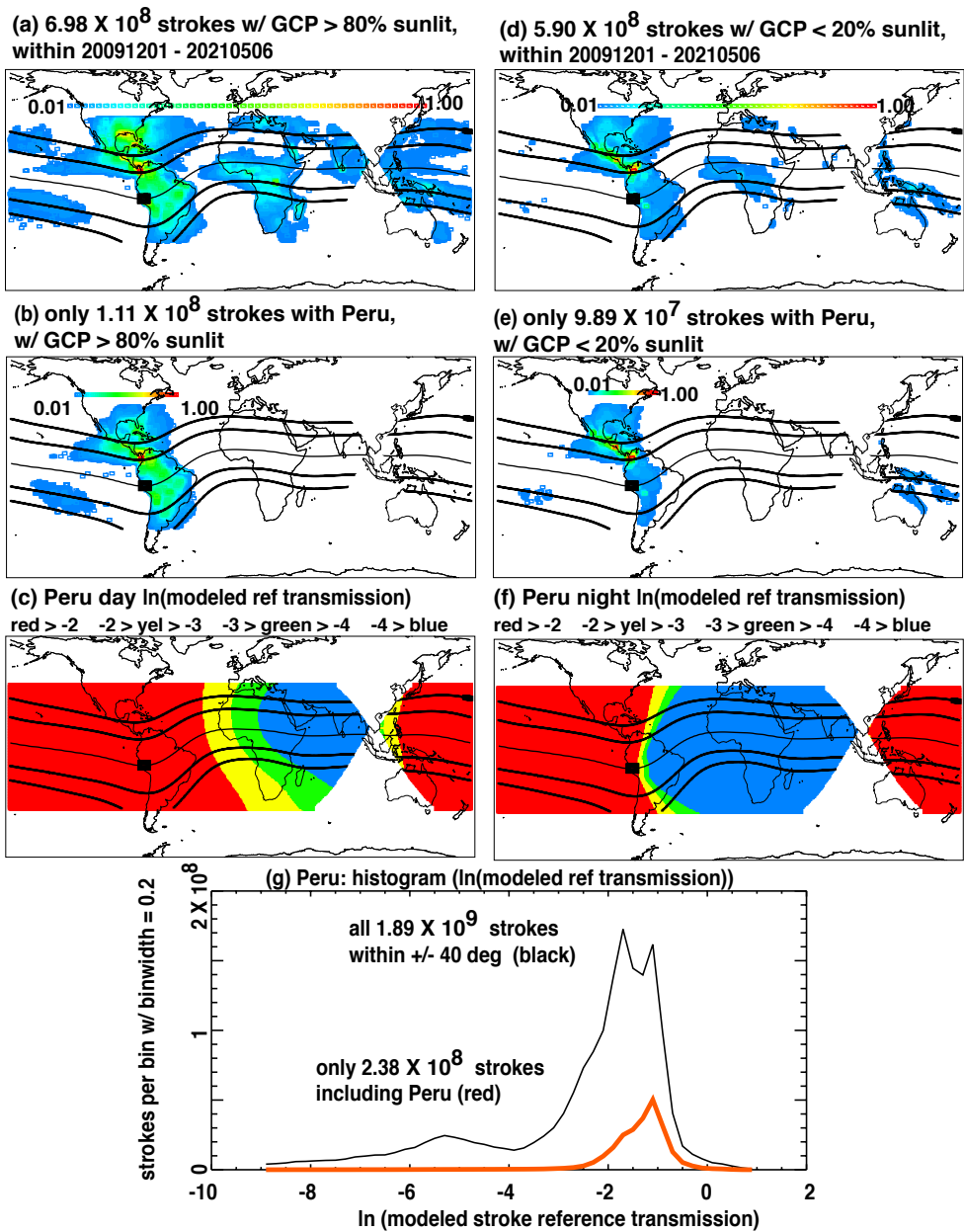
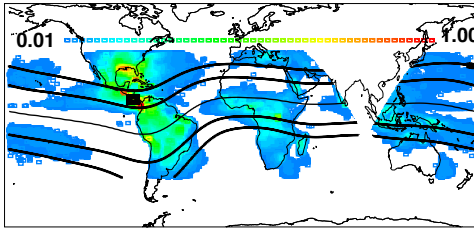
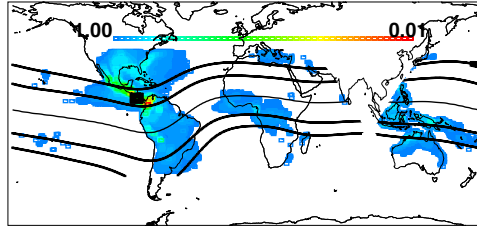


Figure 6: Similar to Figure 4, but for Peru station.

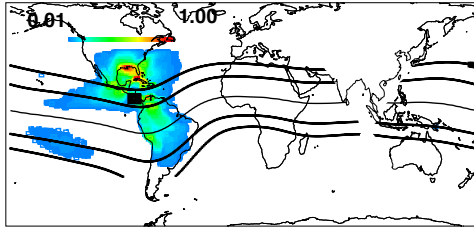
(a) 7.67×10^8 strokes w/ GCP > 80% sunlit, within 20091201 - 20210531



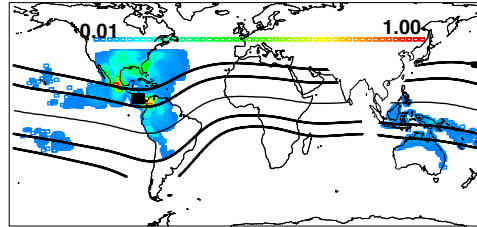
(d) 6.71×10^8 strokes w/ GCP < 20% sunlit, within 20091201 - 20210531



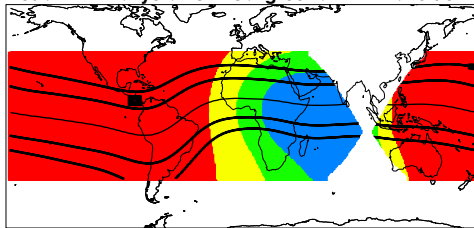
(b) only 1.52×10^8 strokes with Costa Rica, w/ GCP > 80% sunlit



(e) only 1.07×10^8 strokes with Costa Rica, w/ GCP < 20% sunlit



(c) Costa Rica day $\ln(\text{modeled ref transmission})$
red > -2 -2 > yel > -3 -3 > green > -4 -4 > blue



(f) Costa Rica night $\ln(\text{modeled ref transmission})$
red > -2 -2 > yel > -3 -3 > green > -4 -4 > blue

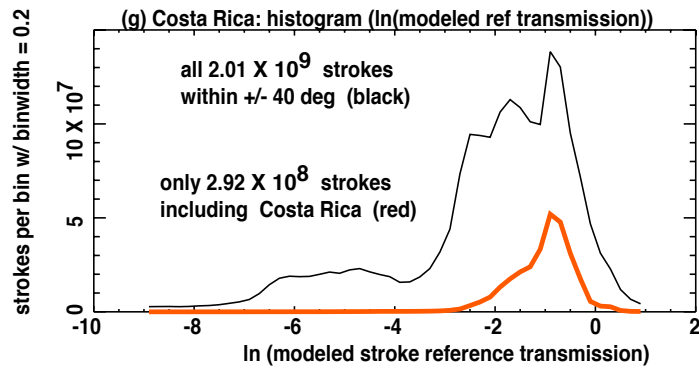
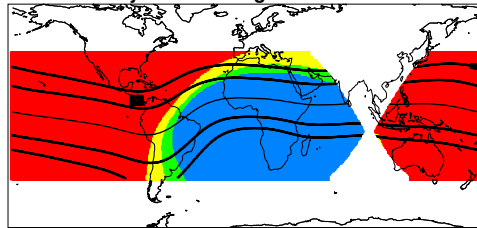


Figure 7: Similar to Figure 4, but for Costa Rica station.

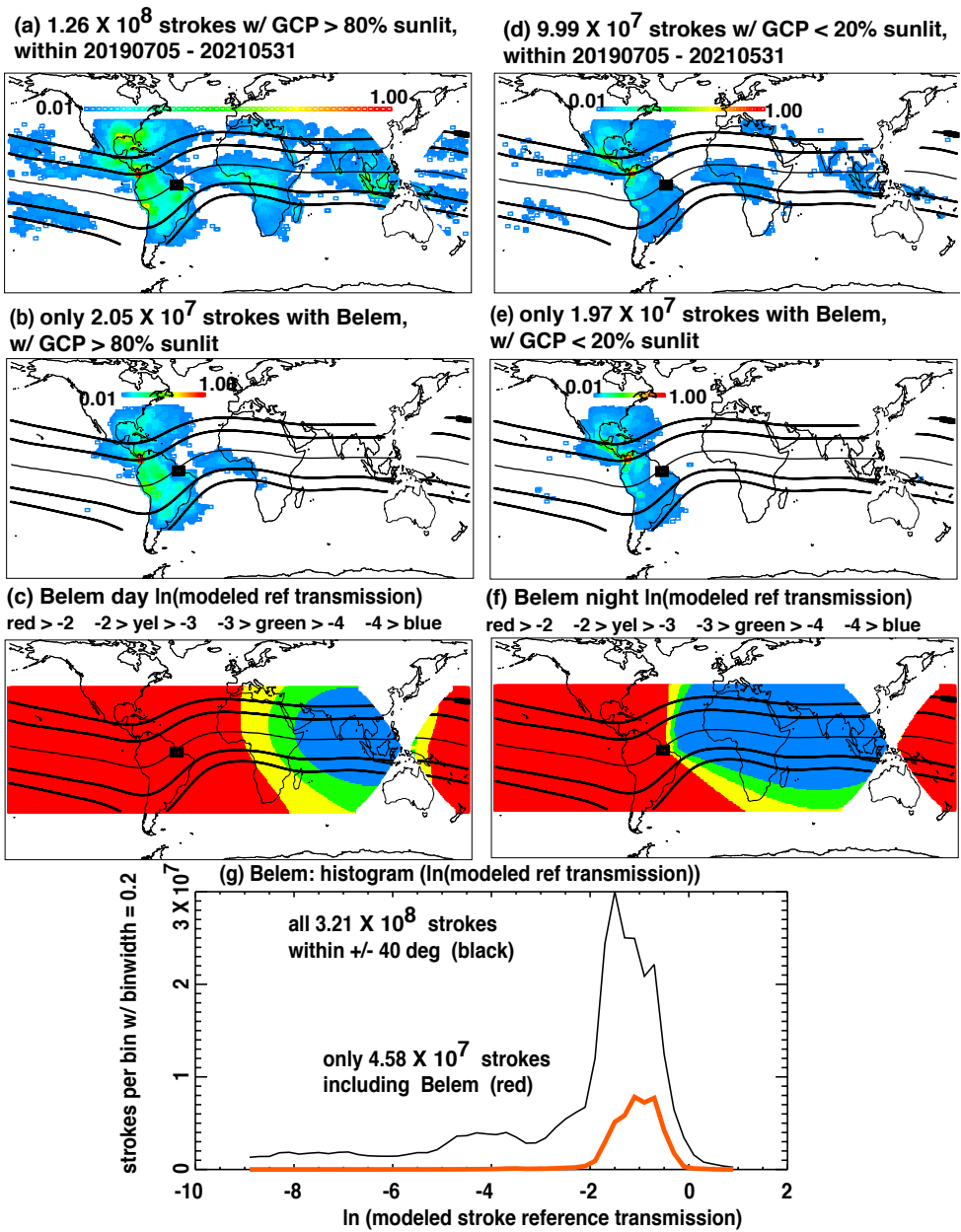


Figure 8: Similar to Figure 4, but for Belem station.

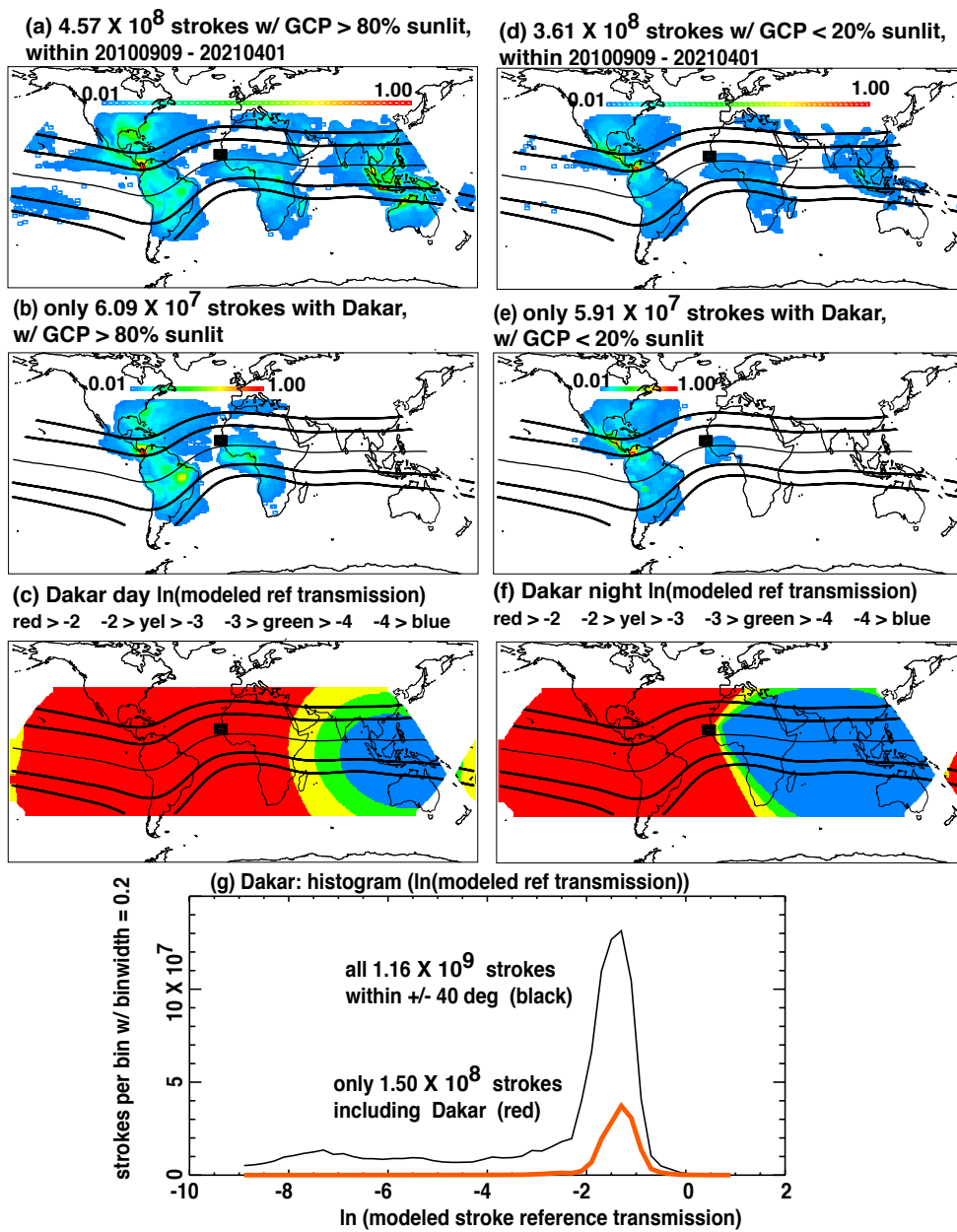


Figure 9: Similar to Figure 4, but for Dakar station.

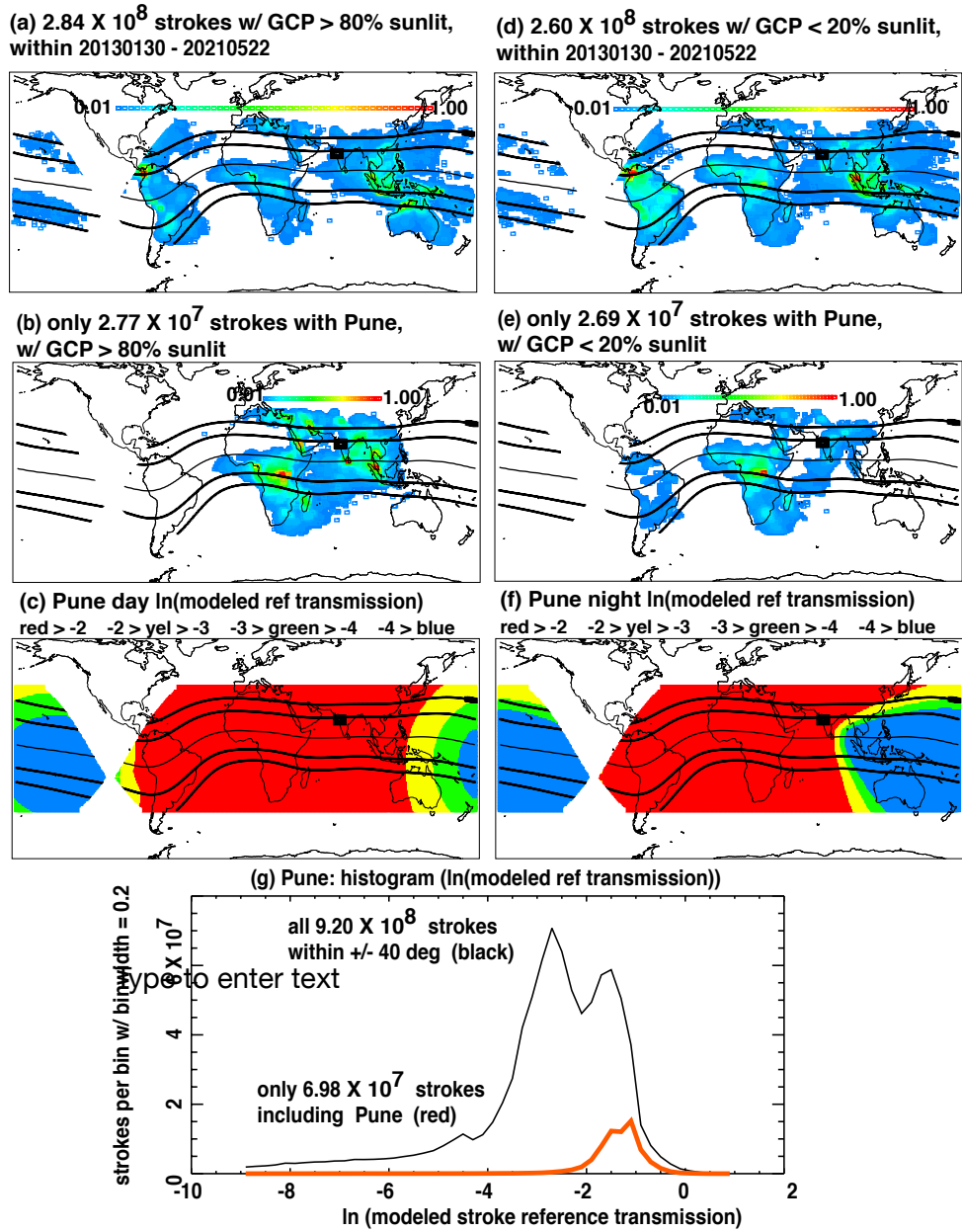


Figure 10: Similar to Figure 4, but for Pune station.

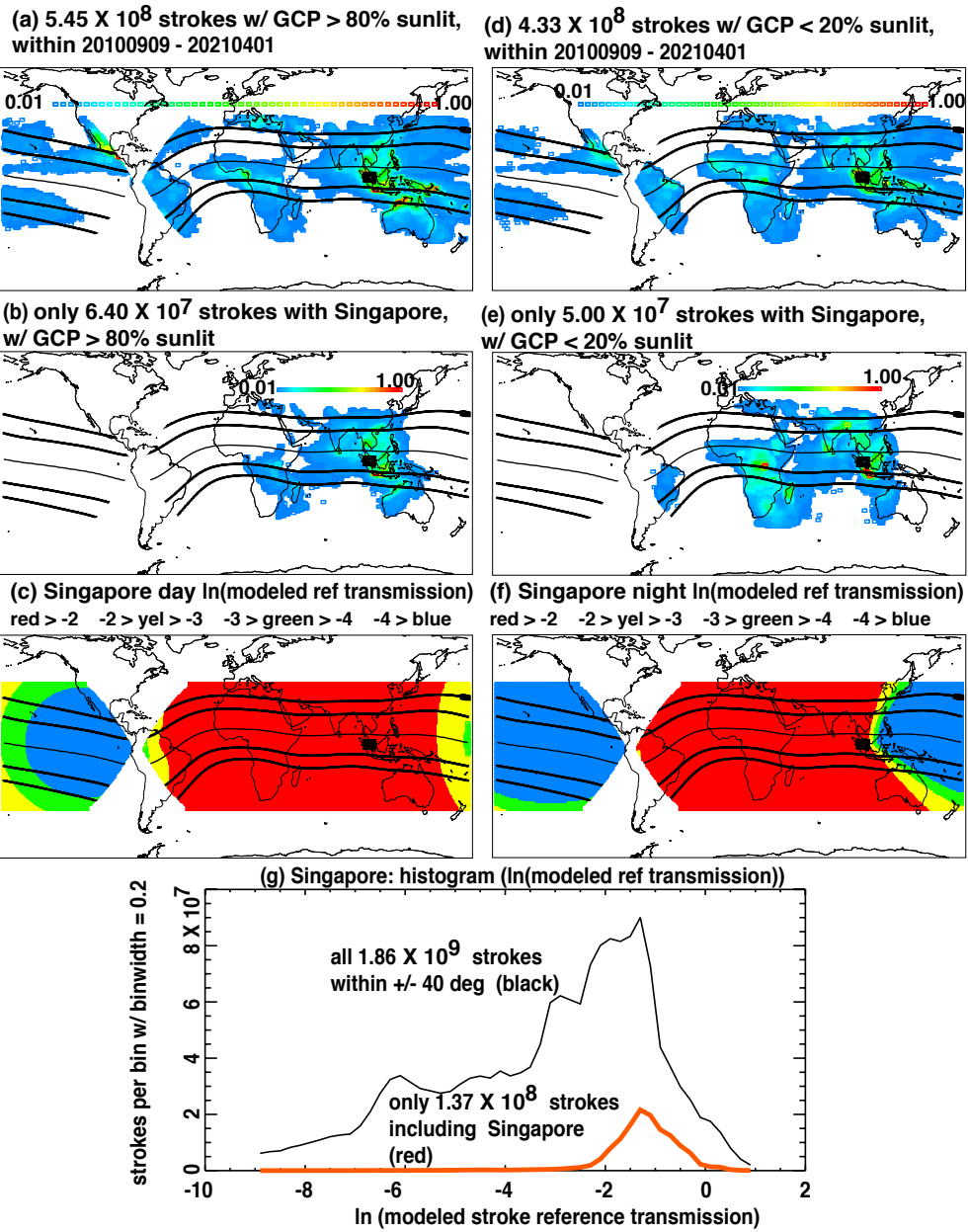


Figure 11: Similar to Figure 4, but for Singapore station.

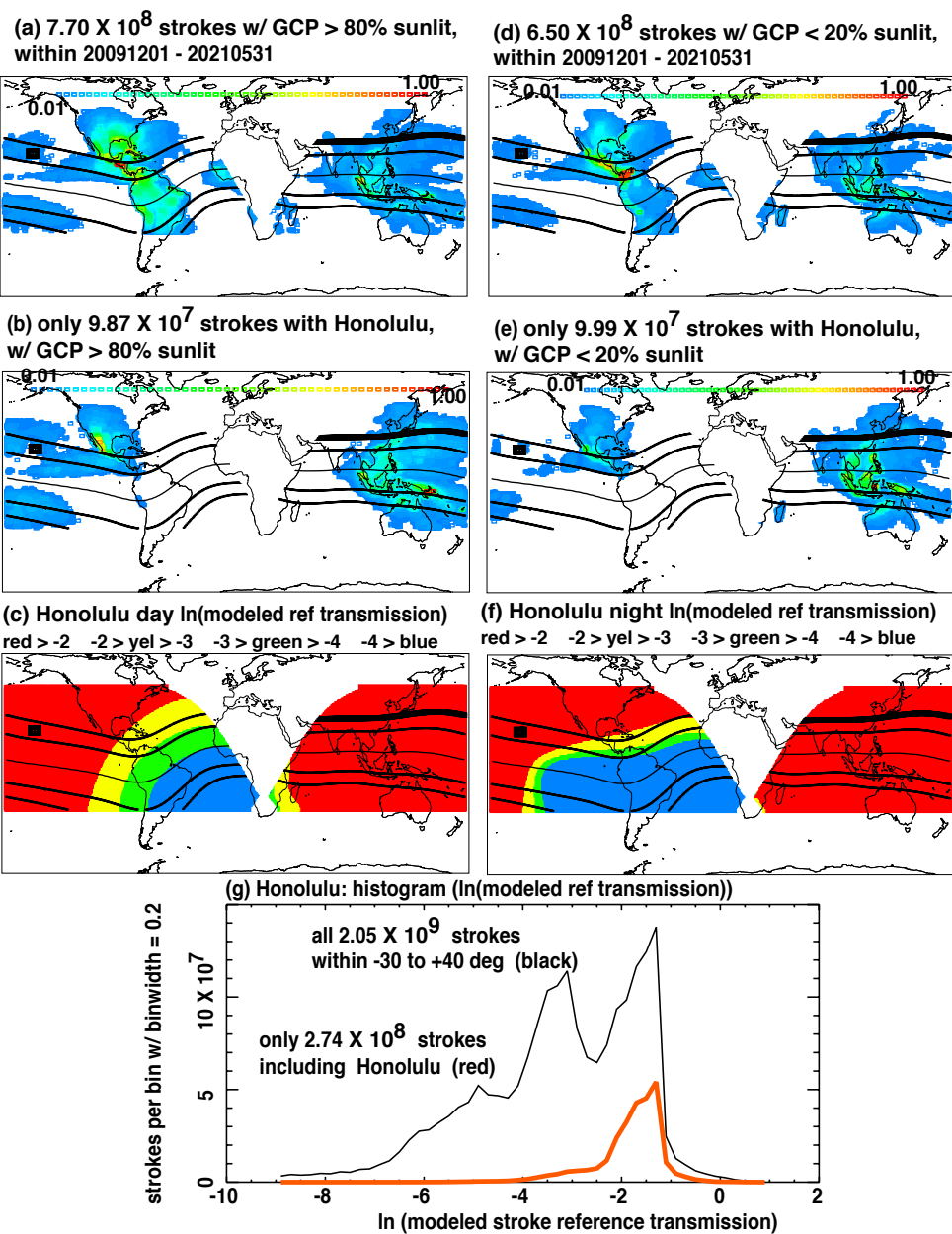


Figure 12: Similar to Figure 4, but for Honolulu station. Note that latitude band is -30 to +50 deg, for this station only.

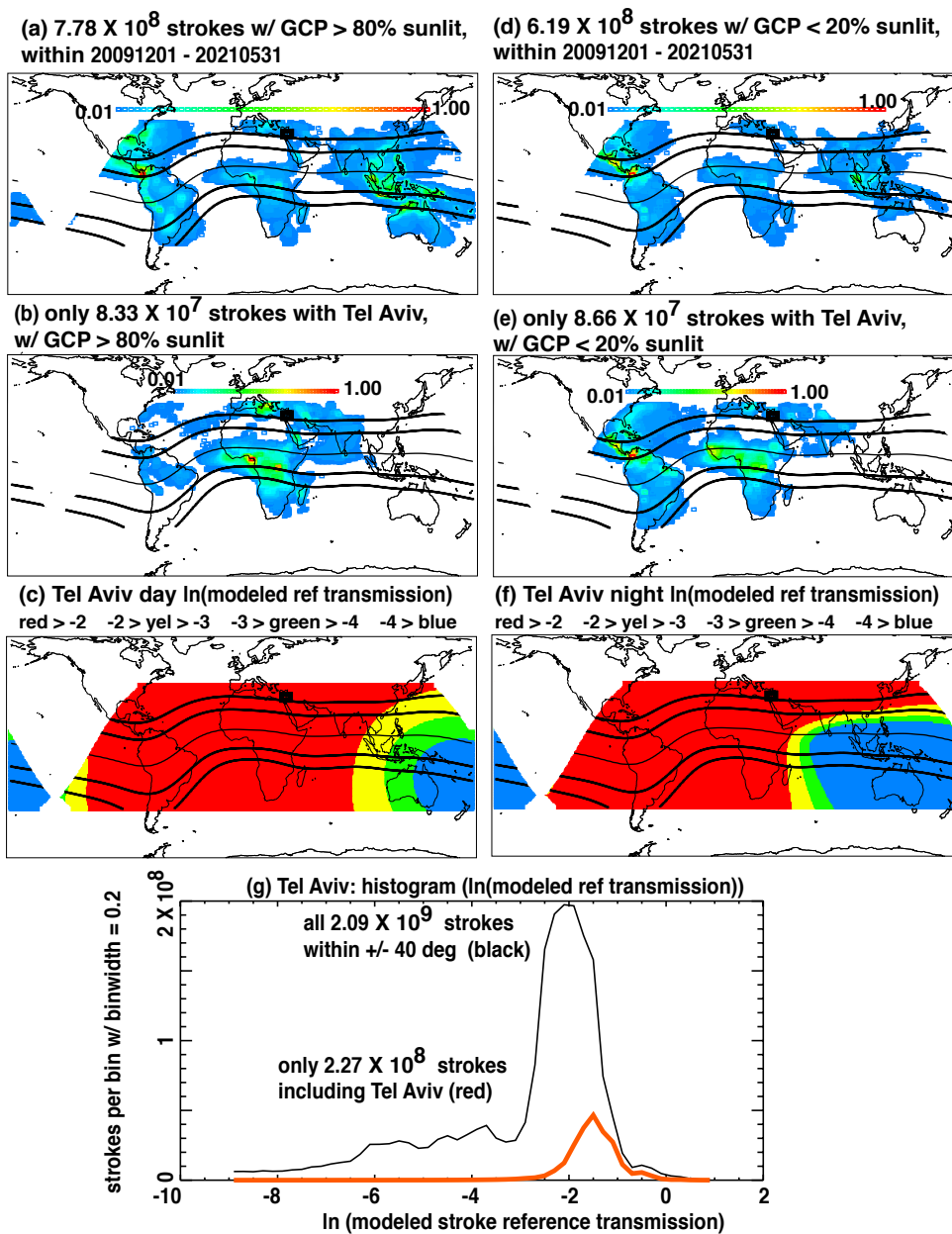


Figure 13: Similar to Figure 4, but for Tel Aviv station.

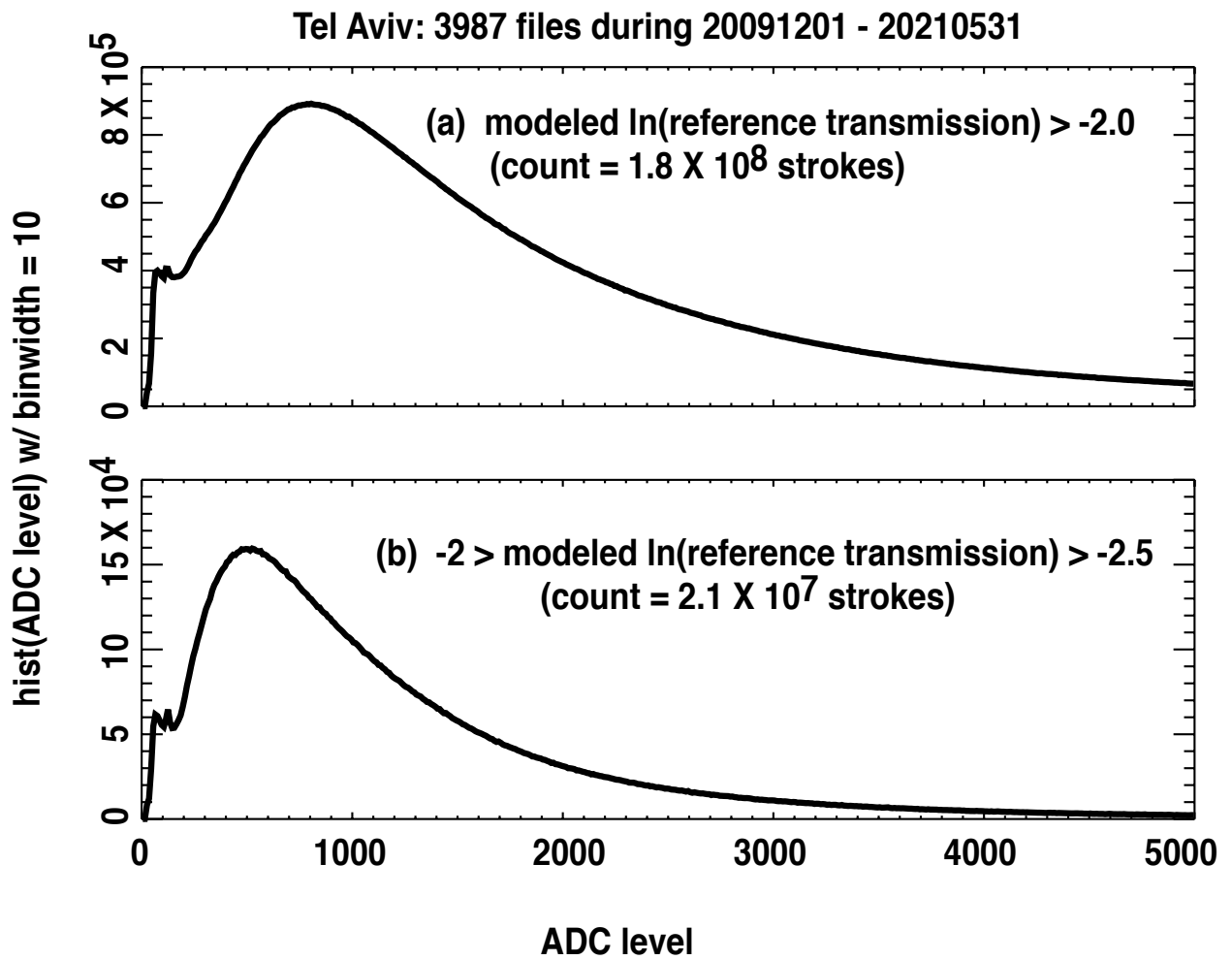


Figure 14: Distribution of raw amplitude (ADC level) for WWLLN-located strokes detected by Tel Aviv station. (a) For logarithmic reference transmission > -2.0 . (b) For logarithmic reference transmission from -2.0 to -2.5 .